2015

TEMPORAL EVOLUTION OF BASAL WATER PRESSURE AND ICE VELOCITY ALONG A 50 KM FLOW LINE TRANSECT OF WESTERN GREENLAND

Patrick Wright
University of Montana - Missoula

TEMPORAL EVOLUTION OF BASAL WATER PRESSURE AND ICE VELOCITY ALONG A 50 KM FLOW LINE TRANSECT OF WESTERN GREENLAND

By

PATRICK J. WRIGHT

M.S. Atmospheric Science, University of Houston, Houston, TX, 2012
B.S. Geology and Environmental Science, University of Oregon, Eugene, OR, 2005

Thesis presented in partial fulfillment of the requirements for the degree of

Master of Science
in Geosciences

The University of Montana
Missoula, MT

December 2015

Approved by:

Sandy Ross, Dean of The Graduate School
Graduate School

Dr. Joel T. Harper, Chair
Geosciences

Dr. Johnnie N. Moore
Geosciences

Dr. Jesse V. Johnson
Computer Science

Wright, Patrick, M.S., Fall 2015 **Geosciences**

Temporal Evolution of Basal Water Pressure and Ice Velocity Along a 50 km Flow Line Transect of Western Greenland

Committee Chair: Joel T. Harper

ABSTRACT

The gradient in hydraulic potential at the ice-bedrock interface beneath the Greenland Ice Sheet (GrIS) dictates the routing and energetics of subglacial water, thereby influencing drainage system characteristics and sliding dynamics. In the ablation zone of the GrIS, a high relief bed and gradients in water pressure in an active subglacial drainage system potentially play a complex role in dictating the hydraulic potential field. Here we present a suite of water pressure measurements collected within thirteen boreholes along a 46 km transect on the western GrIS in order to investigate the sensitivity of the potential gradient field to seasonal evolution and diurnal cycling of basal water pressure. All sites show pressures with similar seasonality, having relatively steady and high values during winter, variable and irregular behavior during spring and fall, and diurnal cycles that can persist for multiple weeks during the peak melt season. Despite much higher variability during the melt season, the median pressure of the summer period is nearly the same as the median pressure of the winter period. Diurnal minimums in water pressure remain above 0.8 of overburden pressure across the transect, except for a single borehole in very near-margin shallow-ice that fell to 0.3 of overburden. We find the mean basal water pressure in western Greenland generally mimics the ice thickness field, but basal drainage processes can superimpose strong gradients over short length scales. Variability of the pressure field due to basal drainage processes can force dynamic changes in the region's hydraulic potential gradient.

High time resolution GPS surface velocity records were collected at 4 sites along the transect during 2011-2015, providing at least two consecutive melt season velocity records at each site, and over-winter records at two sites. Here, I describe methods of GPS station deployment and operation, and data processing and post-processing procedures. Velocity at all sites shows seasonal phases including: a multi-day increasing ramp in the spring from winter background velocities; a period of regular diurnal cycles during mid-summer; and a period of more irregular and variable behavior in the fall, typically characterized by episodic single- or multi-day speedup events. At all sites, linear regression shows decreasing trends in velocity over the melt season. Winter velocity at two sites has magnitude of ~100-120 m/yr, and persists for 9-10 months of the year. In both over-winter records, velocity slowly increases by 10-20 m/yr over the course of the winter.

ACKNOWLEDGEMENTS

This thesis uses measurements collected during five years of field work on the Greenland Ice Sheet by research groups at the University of Montana and the University of Wyoming. Hard work from many individuals provided the invaluable datasets that I have had the privilege to analyze. Joel Harper and Toby Meierbachtol have dedicated countless hours towards fieldwork and logistics, as well as many months of idea development and review of drafts leading to this manuscript. A huge thanks to both of you. Neil Humphrey provided borehole drilling technology, datalogging systems, and valuable scientific insight. Joel Brown did a large amount of groundwork getting TRACK processing routines up and running prior to my arrival with the group, and provided patient assistance while I was learning this software.

Many thanks to the graduate students who have assisted in field work on the icesheet and provided feedback as I worked through the analysis. In particular, thanks to Caitlyn Florentine, Nate Maier, and Ben Hills for contributions to idea development and many days of hard work in the field, and Jacob Downs for answering my random programming and math questions. Additional thanks to all those who labored to make these measurements happen before my arrival with the group.

Thanks to Jesse Johnson and Johnnie Moore for serving on the committee and always having open doors and great insights.

Brendan Hodge, Joseph Pettit, and Thomas Nylen at UNAVCO have provided excellent project support for our GPS installations.

A huge thanks to Thomas Herring and Bob King at MIT for assistance with GAMIT/TRACK troubleshooting.

Russel base station datasets were provided by Sam Doyle and Alun Hubbard at Aberystwyth University.

Also thanks to the hard-working ground crews with NSF science support in Kangerlussuaq, Greenland.

This work is funded by SKB, Posiva, NWMO, and NAGRA; The U.S. National Science Foundation (PP-ANS grants #0909495/#1203451); and, NASA (grant #NNX11AM12A).

TABLE OF CONTENTS

Chapter 1

Measured basal water pressure variability of western Greenland Ice Sheet: Implications for hydraulic potential

Preface

This chapter is written in a journal article format, intended for submission for publication in 2016. Figures are shown in-line with the text, and tables are listed at the end of the chapter. (At the time of this thesis, Section 1.6, Supplementary Figures, is not intended to be included with the journal article submission.)

1.1 Introduction

The subglacial drainage system imparts a key control on the sliding speed of the Greenland Ice Sheet (GrIS) by dictating the variability of basal water pressure and areas of coupling between the ice sheet and its bed. The drainage system evolves seasonally [e.g., *Hoffman et al.*, 2011] in response to input of surface melt, which rapidly reaches the bed via moulins and crevasses [*Das et al.*, 2008; *Catania and Neumann*, 2010; *McGrath et al.*, 2011]. Active drainage systems likely evolve inward from the margin [e.g., *Chandler et al.*, 2013], establishing networks of channelized and distributed drainage elements which define drainage basin areas. The routing of water in these networks is set by the direction and magnitude of the hydraulic potential gradient.

Total hydraulic potential at the ice-bed interface is comprised of an elevation potential and a pressure potential. Elevation potential is dictated by topographic relief, and the pressure

potential is driven by water pressure at the bed. Because water pressure is generally poorly constrained, it is commonly assumed to be a spatially invariant fraction of ice overburden pressure [e.g., *Shreve*, 1972; *Cuffey & Paterson*, 2010]. In this scenario, differentiation of the potential field yields a hydraulic potential gradient ($\nabla\emptyset_h$) for static pressures:

$$-\nabla\emptyset_h = -\rho_i g\left[\frac{P_w}{P_i}\nabla S + \left[\frac{\rho_w}{\rho_i} - \frac{P_w}{P_i}\right]\nabla B\right], \quad (1)$$

where ∇S is the surface elevation gradient, ∇B is the bed elevation gradient, P_w and P_i are basal water pressure and ice overburden pressure, respectively, ρ_w and ρ_i are water density and ice density, respectively, and g is acceleration due to gravity.

Equation 1 relies upon the assumption that water pressure gradients are directly related to changes in surface and bed topography: i.e. situations where the water pressure field essentially mimics the ice thickness field. However, large pressure gradients in the subglacial drainage system are often induced by basal processes such as water flux imbalances, ice wall melt-back, creep closure of the ice roof, and cavity opening from sliding. Pressure gradients have been observed by direct measurement [e.g., *Meierbachtol et al.*, 2013; *Andrews et al.*, 2014] implying active basal processes in Greenland, and have also been inferred from physics-based modeling of drainage system evolution [e.g., *Hewitt et al.*, 2012; *Hewitt*, 2013; *Werder et al.*, 2013]. Drainage system effects are sometimes considered by allowing the water pressure in Equation 1 to deviate from the pressure

generated by the weight of the ice, but only by a constant value with no gradients from basal processes [e.g., *Lindbäck et al.*, 2015].

At long regional [e.g., *Tedstone et al.*, 2014; *Lindbäck et al.*, 2015] and ice sheet scales [*Lewis and Smith*, 2009; *Liston and Mernild*, 2012; *Livingstone et al.*, 2013], Equation 1 is assumed to be valid and applied to the GrIS to estimate drainage basin size, which controls the spatial distribution of water and sediment flux. However, such computations require definition of the water pressure across the basin which strongly influences the relative role of surface and bed topography in calculated potential gradients, and resulting drainage basin characteristics [*Lindbäck et al.*, 2015]. The critical role of water pressure is illustrated by a comparison of the ratio of the surface gradient multiplier $[P_w / P_i]$ to the bed gradient multiplier $[(\rho_w / \rho_i) - (P_w / P_i)]$ in Equation 1 under varying water pressure (Fig. 1.1). The relationship is highly nonlinear such that small changes in water pressure at values near overburden can result in large changes in the hydraulic potential gradient if the disparity between surface and bed slopes is substantial. The influence of pressure on the potential gradient field is further complicated by the fact that water pressure may vary in time due to seasonally and diurnally varying melt input.

Recent development of bed DEMs using radar and mass conservation techniques have revealed basal topography beneath the GrIS that is much more variable than previously assumed [*Bamber et al.*, 2013; *Lindbäck et al.*, 2014; *Morlighem et al.*, 2014]. In particular,

the ablation zone of the western GrIS is characterized by reaches with steep-walled bedrock troughs. The ice surface remains relatively smooth in these regions, with shallow surface slopes and only muted expressions of bedrock topography, resulting in highly variable ice thickness.

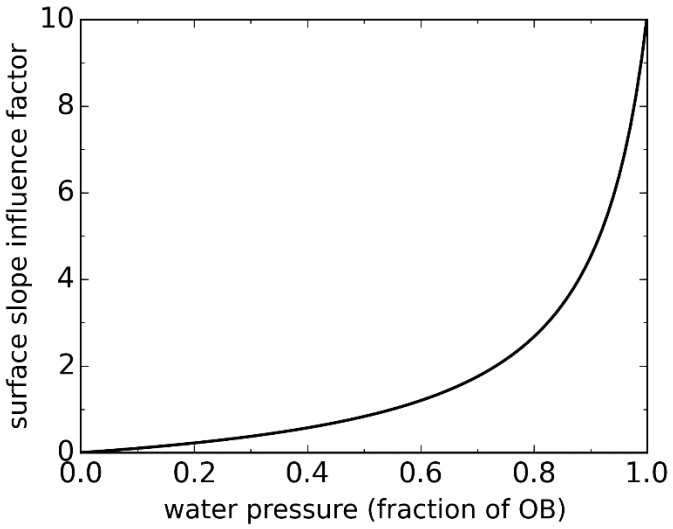

Fig. 1.1 Influence of ice surface slopes on the total hydraulic potential gradient as a function of basal water pressure. ("Surface slope influence factor" of 1 indicates that surface slopes and bed slopes contribute equally to the total potential gradient. A factor of 10 indicates that the surface is 10x more influential than the bed.)

The hydraulic potential gradient at the bed of GrIS is therefore expected to be strongly controlled by details of the water pressure field and its changes in time: $\nabla \phi_h$ should be sensitive to small changes in the magnitude of pressure because of steep bed slopes, and $\nabla \phi_h$ should be sensitive to non-overburden related pressure gradients which arise from basal processes and seasonal development of a basal drainage system. Our working knowledge of these details, however, is quite limited. Early borehole measurements in GrIS identified pressure near overburden, but records typically spanned only a few days

[*Thomsen and Oleson*, 1990, 1991; *Thomsen et al.,* 1991; *Iken et al.*, 1993]. Only recently have measurements become more temporally and spatially extensive, demonstrating diurnal cycles and seasonality in both borehole and moulin-measured water pressure [*Luthi et al.*, 2002; *Meierbachtol et al.*, 2013; *Andrews et al.*, 2014; *van de Wal et al.*, 2015]. Despite the increasing fidelity of topographic data, a lack of constraints on basal water pressure continue to invoke large uncertainty in hydraulic potential gradients.

In this study we use measurements collected in thirteen boreholes to assess temporal and spatial scales of basal water pressure variability along a 46 km transect in western Greenland. Borehole records collected during 2010-2015 span summer and winter periods and include six sites ranging from near-margin to inland conditions. As such, the records permit assessment of spatial pressure gradients at the site- to regional-scale as well as temporal changes over daily and seasonal periods. We use these results to examine the sensitivity of the potential gradient field to variability in water pressure.

1.2 Methods

1.2.1 Borehole measurements

Boreholes were drilled using hot water methods at six locations along a transect moving inland from Isunnguata Sermia, on the southwest margin of the GrIS (Fig. 1.2). For the borehole locations described below, all distances inland are reported as distance from the terminus of Isunnguata Sermia. Three boreholes are located at a near-margin location

(sites GL10-1 and GL10-2). These sites are approximately 12 km inland, however they are located very near the lateral margin at a point where Isunnguata Sermia exits the main body of the ice sheet. Boreholes GL10-2B and GL10-2C are co-located within 10 meters, and are approximately 1 km from the lateral margin (ice depth ~150 m), and borehole GL10-1D is located approximately 450 meters from the lateral margin (ice depth ~100 m).

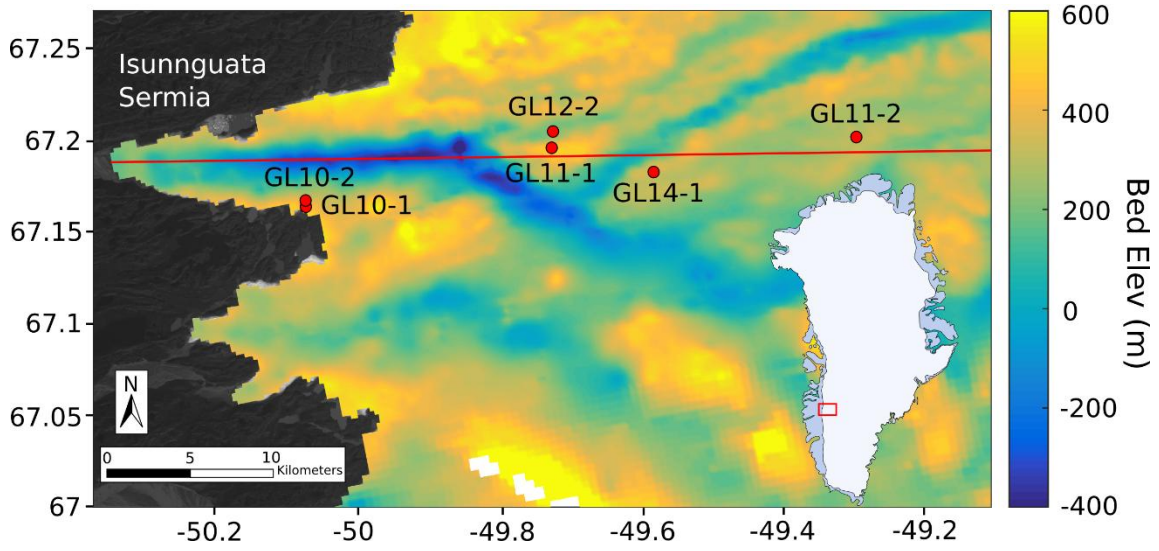

Fig. 1.2. Locations of borehole sites along the study transect in western Greenland, shown with 250-meter resolution bed topography (Lindbäck et al., 2014). Red line indicates the profile line for Figure 1.8.

Sites GL11-1 and GL12-2 are located approximately 27 km inland. GL11-1 overlies a ridge in bedrock topography (ice depth ~460 m), and is located approximately 1 km from site GL12-2, which overlies a bedrock trough (ice depth ~700 m). Boreholes at these sites are co-located within 20-30 meters. Site GL14-1 is located approximately 33 km inland (ice depth ~670 m), with two boreholes co-located within ~150 meters. This site overlies a high plateau in bedrock topography with a major northeast-southwest trending bedrock

trough located north of the site. Site GL11-2 is located approximately 46 km inland (ice depth ~820 m), with two boreholes co-located within 20 meters. GL11-2 is located ~30 km below the long term equilibrium line altitude (ELA) [*van de Wal et al.*, 2012]. Distance inland, latitude, longitude, ice depth, and length of record for each borehole are listed in Table 1.1.

Hole depth was confirmed with three independent measurements: depth marks on the drill hose, depth marks on instrumentation cable lowered down the borehole, and depth from a digital odometer on the drill. From these measurements, we estimate the accuracy of reported borehole depths to be <1.5% of total ice thickness (±2 m for margin locations, ±12 m for inland locations). Additional details of borehole drilling and instrumentation methods are described by Meierbachtol et al. [2013] (supplementary material).

Boreholes were instrumented near the bed with pressure transducers logging at 5 or 15 minute intervals during summer and 15 or 30 minute intervals during winter. Pressure transducers were lowered to a position ~25-50 cm above the bed, with boreholes then freezing shut except near the bed where temperature measurements at each site show the ice is temperate [*Harrington et al.*, 2015]. The length of pressure records is limited by the connection of the sensor cables, which can fail due to stretching or rupture from crevassing at near-margin locations.

Water pressure is most commonly reported in this study as a fraction of overburden (OB) pressure. For all calculations, we assume an ice density of 910 kg/m^3. However, ice density can vary due to air bubbles, liquid water, or debris and impurities, and can commonly range 880 – 917 kg/m^3 [*Cuffey & Paterson*, 2010]. Uncertainty is analyzed for the combined maximum and minimum errors due to pressure transducer resolution (±0.1 meters), ice depth measurements, and ice density. Resulting uncertainty in scaled overburden calculations varies slightly as a function of ice depth, with a maximum range from all error sources for our deepest borehole of -0.022 OB to +0.047 OB. This uncertainty is predominantly a function of the possible range in values for ice density. If the range of ice density is constrained to 900-917 kg/m^3, the maximum range in uncertainty is reduced to -0.022 OB to +0.026 OB.

1.2.2 Statistical techniques

Box plots were generated to summarize seasonal and diurnal water pressure datasets. For seasonal analysis, seven records encompass part or all of a single melt season, and five records include winter data, with four of these records spanning slightly more than a year (Table 1.1). For borehole records spanning part or all of a single melt season, box plots represent all data contained in the record, whereas the five records with winter data have been separated into box plot pairs for characteristic winter and melt season records, respectively. This approach allows for separate analysis of melt season and winter pressures, and allows calculation of an annual weighted mean pressure that incorporates data from all boreholes.

The borehole water pressure records show non-normal distributions, thus we use dataset medians as an indicator of central tendency for the temporal scale of interest. An annual mean value is calculated by weighting the mean melt season median among all boreholes to 3.5 months (0.29 yr), and the mean winter median among five boreholes to 8.5 months (0.71 year). This weighting scheme allows the use of all records in the dataset, using a time span of characteristic melt season data for weighting that is generally consistent among all boreholes, from approximately June 15 to October 1. All reported median values are calculated from data re-sampled to common time intervals (5 minute or 15 minute for melt season records, and 15 minute or 30 minute for winter records).

1.3. Water Pressure Results

1.3.1. Seasonal phases

Borehole water pressure throughout the transect shows characteristic seasonal phases, with a clear distinction between melt season and winter behavior (Fig. 1.3). Winter water pressure is characterized by a confined range of pressure that dominates for nearly eight months of the year. Pressure during winter commonly shows low-frequency variability over weeks and months, although in one case bimodal behavior is observed, with a sudden increase of nearly 0.07 OB (44 meters head) over a five day period (borehole GL12-2C; Fig. 3, C). The winter record for borehole GL14-1C (Fig. 3, E) is an outlier in behavior from

other winter records, showing two cycles with a range of 0.12 OB (75 meters head) evolving over 2-3 month periods.

The melt season includes an initial spring phase, a period of regular diurnal cycles, and a fall "shutdown" phase. In the spring the winter-melt season transition is distinct, characterized by a sudden sharp increase in pressure usually occurring in early June. In two boreholes (GL11-1A, GL12-2A) the spring activation event is 0.005-0.02 OB in magnitude (3-6 meters head), which is subsequently followed within days or weeks by further increases to pressures near overburden. The spring event in two boreholes, GL12-2C and GL12-2D, consists of a single rapid increase of 0.03-0.04 OB (17-26 meters head). Spring events often record the maximum pressure values for an annual period; for example, the spring activation event in 2013 for borehole GL12-2C (Fig. 1.3C) reaches a maximum pressure of 1.08 OB.

The period of summer diurnals weakens and becomes more irregular in late August or September, defining a transition to fall behavior. The fall phase is often characterized by an evolution to higher pressures and a dampening of diurnal variability over a period of weeks until a relatively constant pressure is reached and sustained into winter, indicating the melt season-winter transition.

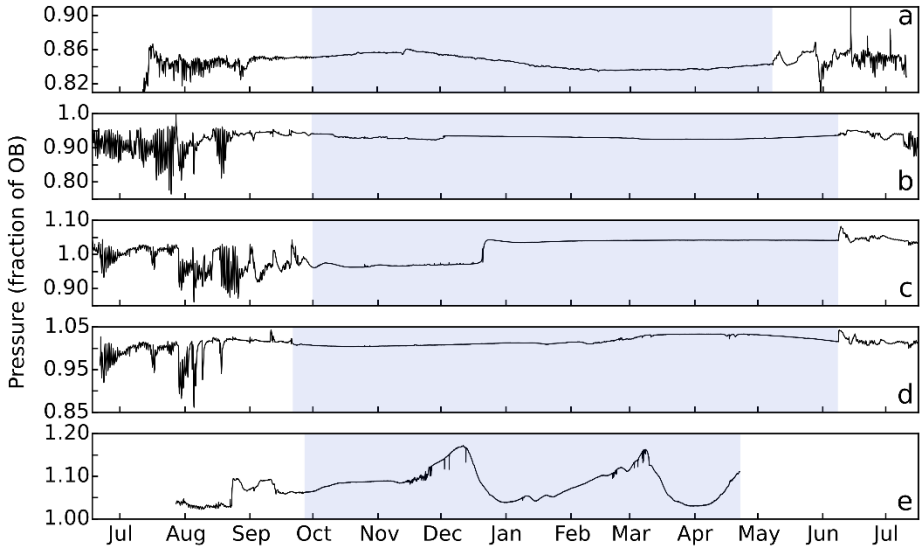

Fig. 1.3. Annual water pressure records from boreholes GL11-1A (Panel A), GL12-2A (Panel B), GL12-2C (Panel C), GL12-2D (Panel D), and GL14-1C (Panel E). The characteristic winter period for each record is shaded in blue.

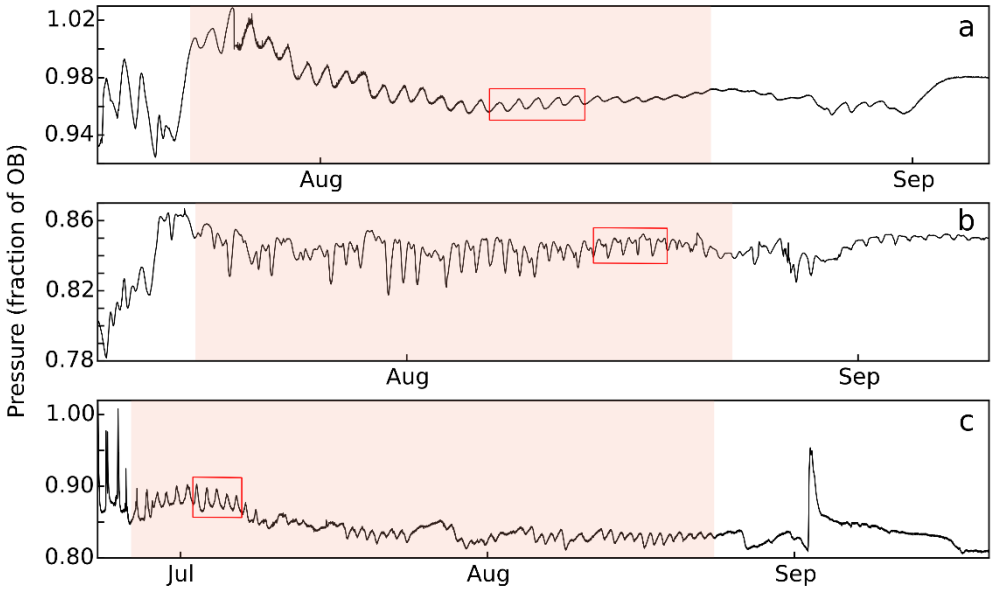

Fig. 1.4. Melt season water pressure records for boreholes GL11-2D (Panel A), GL11-1A (Panel B), and GL10-2B (Panel C). The period representing "summer diurnals" for each record is shaded in red. Five day periods selected for diurnal analysis (Fig. 1.5) are indicated with red boxes.

1.3.2. Diurnal cycles

All boreholes show periods of regular diurnal variability during mid-summer (Fig. 1.3, 1.4). However, the magnitude and range of diurnal swings can be highly variable between boreholes. With exception to near-margin borehole GL10-1D (discussed separately below), the remaining twelve-borehole suite shows diurnal cycles that are predominantly confined to a distinct range of 0.8 - 1.1 OB (Fig. 1.6).

Once diurnal cycles are established, minimum pressures reached during July or August are typically the lowest pressures of the annual record for a borehole. A low pressure of 0.76 OB reached during late July in borehole GL12-2A (Fig. 1.3, B) defines the minimum pressure recorded in the twelve-borehole suite. However, we see no evidence for consistent sub-seasonal decreasing trends in the magnitude of diurnal maximum or minimum pressures. Periods of diurnal cycles can show occasional multi-day trends of slightly increasing *or* decreasing pressure, but each pressure record remains constrained within the range throughout the melt season (Fig. 1.6).

Pressure data from borehole GL10-1D are unique from all other records. Located just 450 meters from the lateral margin of Isunnguata Sermia with an ice depth of 99 meters, water pressure records at this site show large diurnal pressure swings (68 meters head), reaching a melt season minimum near 0.3 OB, yet with daily maximum pressures remaining above overburden throughout the melt season (Fig. 1.6, light grey record).

Despite low minimum pressures, the median pressure for the entire record remains high at 0.86 OB, largely due to diurnal maximums consistently near overburden throughout the melt season.

The time-distribution of water pressure during diurnal cycles does not necessarily follow a perfect sinusoid, as is often modeled [e.g., *Dow et al.*, 2014]. For example, three distinct end-member types of diurnal cycles were observed: a symmetric mode where time is equally partitioned across the pressure range; a high-pressure dominated mode, where higher pressures occupied a greater fraction of the day; and a low-pressure dominated mode, where more of the day was occupied by lower pressure (Fig. 1.5). Each of these three case studies shows a similar range in diurnal pressure of approximately ± 3 meters head.

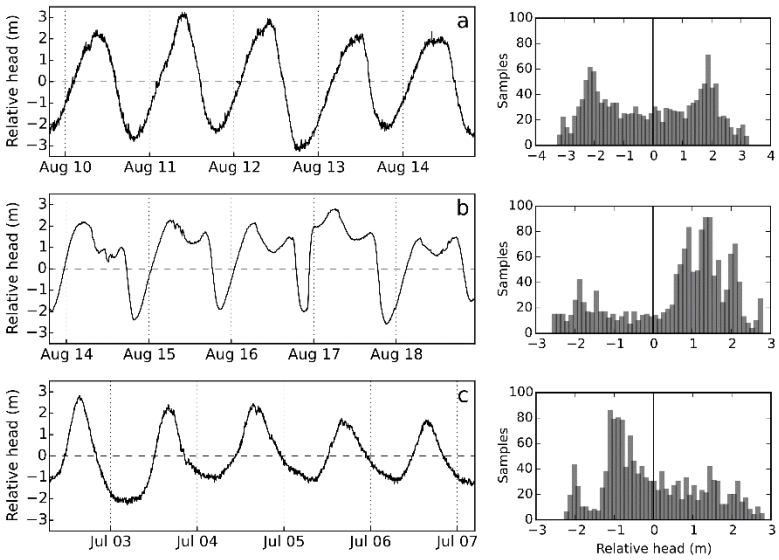

Fig. 1.5. Three modes of diurnal variability, corresponding to five day periods indicated in Figure 1.4. Panel A represents a symmetric mode from site GL11-2D. Panel B represents a high-pressure dominated mode from site GL11-1A. Panel C represents a low-pressure dominated mode from site GL10-2B. Corresponding histograms show distribution of data.

Histograms based on five-day detrended periods demonstrate the difference between the three cases in the time-distribution of water pressure. In the symmetric mode (Fig. 1.5, Panel A), water pressure resides at high and low magnitudes for approximately equal portions of the diurnal cycle (51% below, 49% above). In the high-pressure dominated mode (Fig. 1.5, Panel B) water pressure is sustained above the median value for 73% of the period, and in the low-pressure dominated mode (Fig. 1.5, Panel C) pressure remains below the median value for 58% of the period. There is no clear dominance of one type of behavior across the transect, however the mode that is established for an individual borehole tends to stay consistent throughout the summer diurnal period (Fig. 1.4).

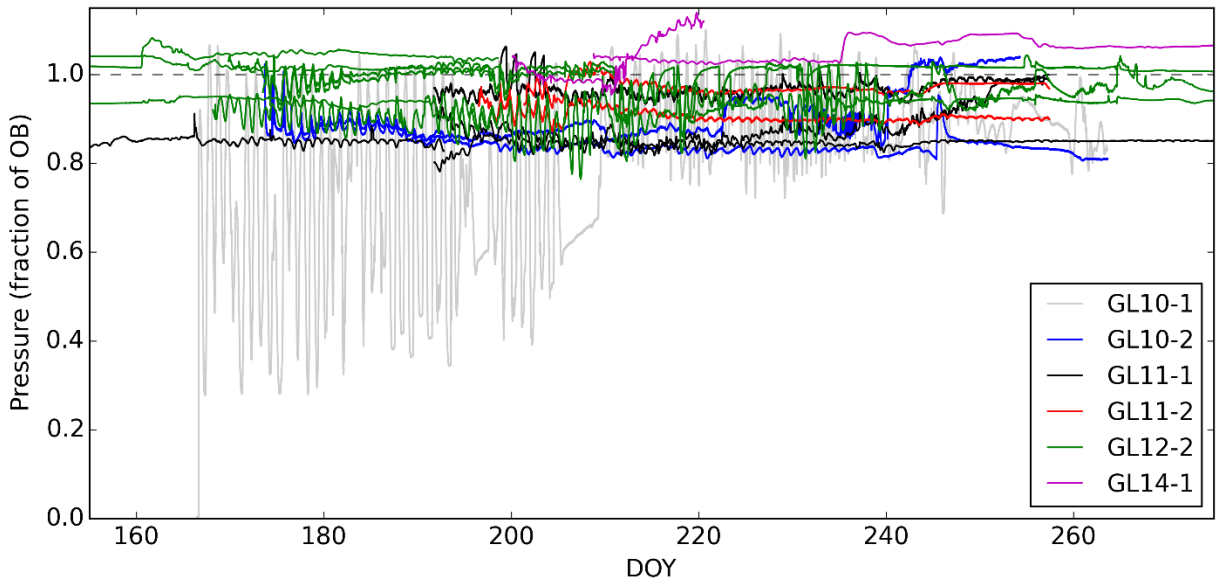

Fig. 1.6. Melt season basal water pressure records from all boreholes. With the exception to the near-margin, shallow-ice borehole GL10-1D (transparent grey record), all pressure records throughout the transect are confined to a range of approximately 0.8 – 1.1 of overburden pressure.

1.3.3. Spatial Gradients

Our measurements demonstrate that substantial gradients in the fraction of overburden pressure can exist between adjacent boreholes spaced 10s to 100s of meters apart. Pressure differences arise from hole-specific temporal fluctuations occurring over time periods of hours to weeks. For example, boreholes GL11-2B and GL11-2D are co-located within 20 m and both boreholes show consistent diurnal cycles (Fig. 1.7). However, the two pressure records have different magnitudes throughout the melt season by ~0.06 of OB (~40 meters head). This difference in head represents a water pressure gradient of ~20 kPa/m. Because the ice thickness measured directly in the boreholes differs by only 6 meters, these gradients can only be attributed to basal drainage system processes (the overburden pressure gradient is an order of magnitude less).

Boreholes spaced 10s to 100s of m apart can show differences within the same range of values (~0.8 to >1.0 OB) as sites 10s of km apart, when expressed as a fraction of the overburden pressure (the exception is the near margin hole, which we argue in section 1.4.1 is a special case). The absolute water pressure, however, shows very large changes across the study domain driven by overall changes in ice sheet thickness (Fig. 1.8), with gradients averaging 0.16 kPa/m as ice thins towards the margins. In addition, very large changes in ice thickness exist along walls of steep bedrock troughs, where pressure gradients over 100s of meters can be nearly 20 times greater than the overall transect gradient.

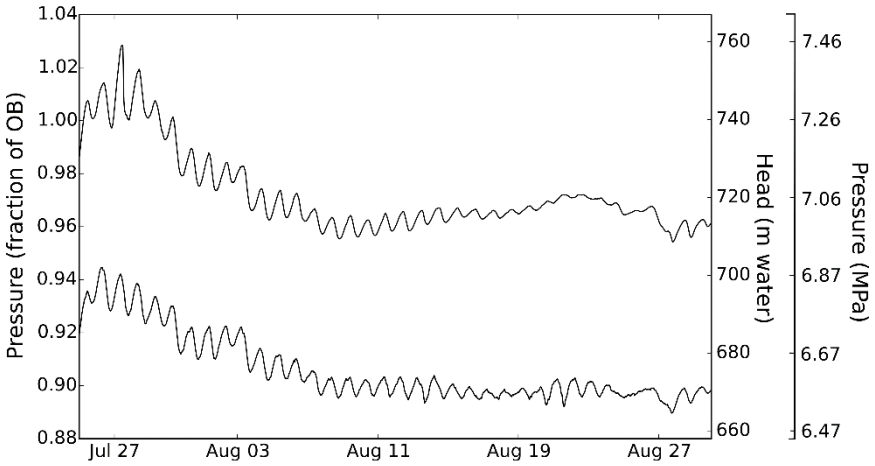

Fig. 1.7. Pressure records during 2011 from boreholes GL11-2B (lower record, ice depth 821 m) and GL11-2D (upper record, ice depth 815 m), located 46 km inland from the terminus of Issunguata Sermia. Boreholes are co-located at the site within 20 meters.

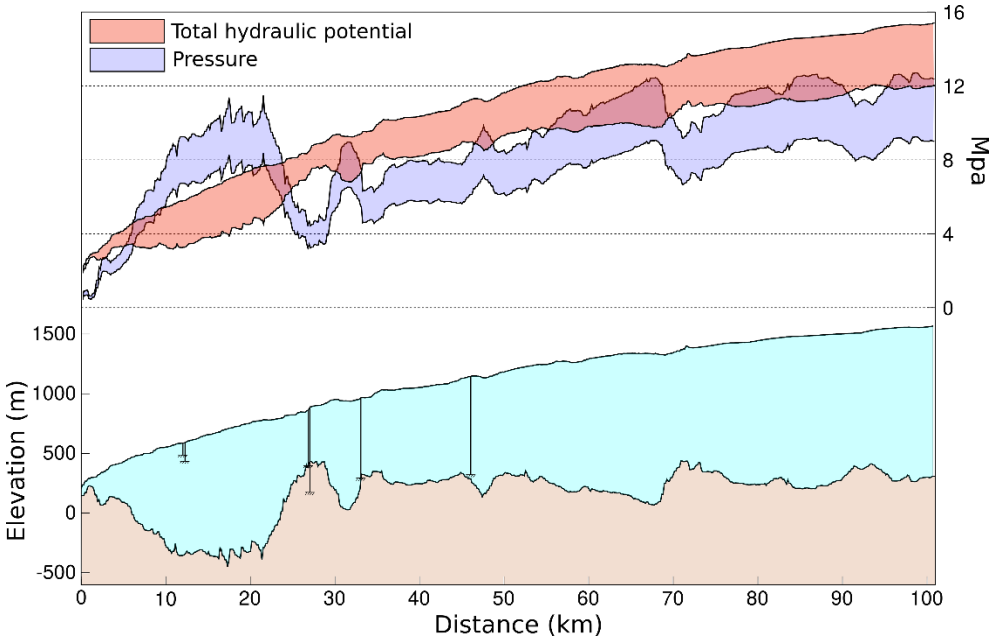

Fig. 1.8. Gradients in total hydraulic potential and basal pressure for the transect line shown in Figure 1.2, extending to 100 km inland. Ice surface and bed topography along the profile are shown for context. The shaded range in both pressure and total hydraulic potential is constrained by the measured borehole pressure range of 0.8 – 1.1 of OB. Changes in basal pressure reflect changes in ice thickness, whereas the total hydraulic potential includes overburden pressure potential and elevation potential. Borehole locations and depths have been projected into the plane of the profile.

1.3.4. Summary statistics

Box plots summarizing all pressure records from each borehole demonstrate no consistent trends in pressure as a function of ice depth or distance inland from the margin (Fig. 1.9). In some cases, boreholes with thicker ice and greater distance inland clearly show higher pressures than more near-margin, shallower locations. For example, boreholes at sites GL12-2 and GL14-1 generally show OB pressures that are higher than at sites GL10-2 and GL11-1. However, evidence for the opposite relationship is equally common. The melt season record of borehole GL10-2C shows consistently higher pressure than two of three boreholes at site GL11-1, despite ice depths that are 300 meters less and a location 15 km nearer to the margin. In addition, both boreholes at the most inland site (GL11-2) show pressures that are lower than all boreholes at site GL14-1 and lower than two of three records at site GL12-2. Similarly, no spatial trends are obvious during the period of diurnal pressure swings alone (Fig. 1.10).

To assess seasonal evolution of water pressure from the winter to the melt season, we separate winter and melt season data for the five boreholes with annual records (indicated with shaded boxplot pairs in Fig. 1.9). For three of these boreholes there is essentially no change from winter to melt season median pressure (<0.01 OB), and in borehole GL14-1C the winter median pressure decreases by only 0.02 OB. This consistent seasonal behavior has exception only in borehole GL12-2C, showing a decrease from winter to melt season median pressure of 0.07 OB resulting from distinct bimodal winter behavior for this borehole which establishes a relatively high median for the winter record (Fig. 1.3, Panel C).

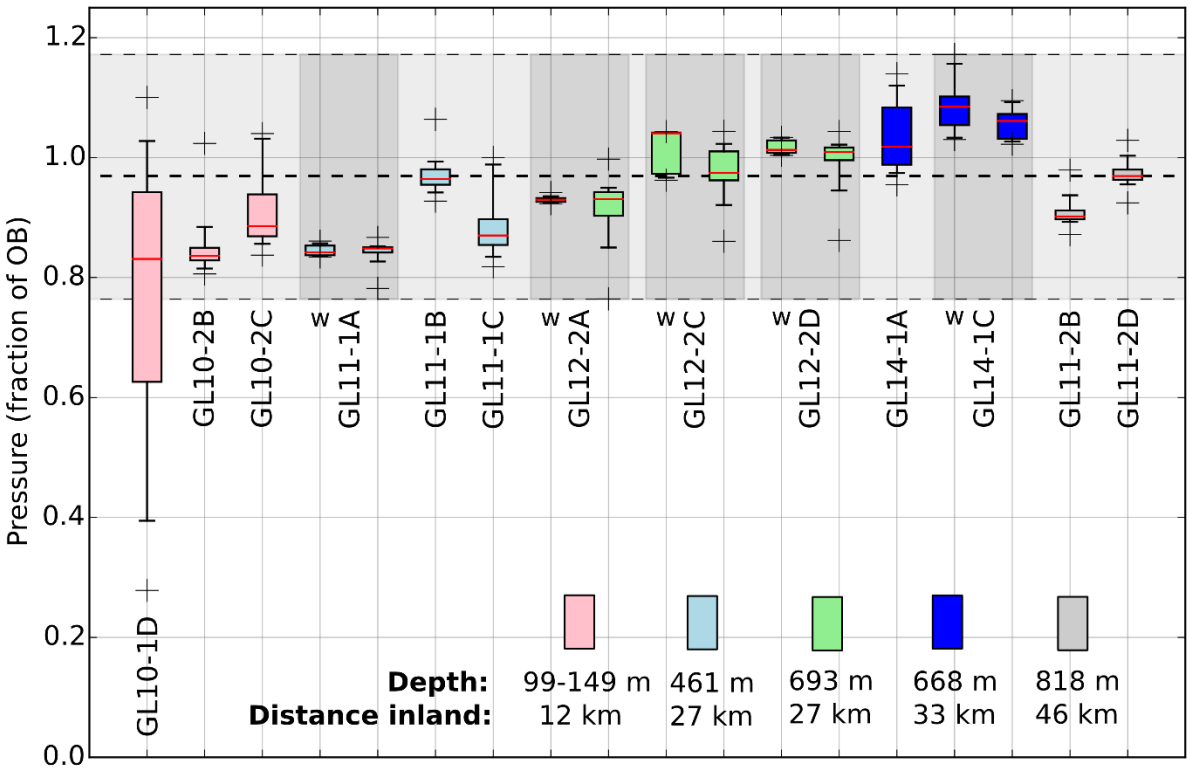

Fig. 1.9. Box plots of basal water pressure data for all boreholes, where box color corresponds to distance inland. For boreholes with over-winter records, corresponding winter and melt season periods are shown in shaded pairs, where winter records are indicated with "w". For boreholes with only melt season records, all data in the record is represented. Box center lines are median, boxes span the 1st and 3rd quartiles, whiskers extend to 5th and 95th percentiles, and crosses indicate max and min points. Bold dashed line is the weighted annual mean for the 12-borehole suite. Shaded region spans the minimum and maximum values of the 12-borehole suite.

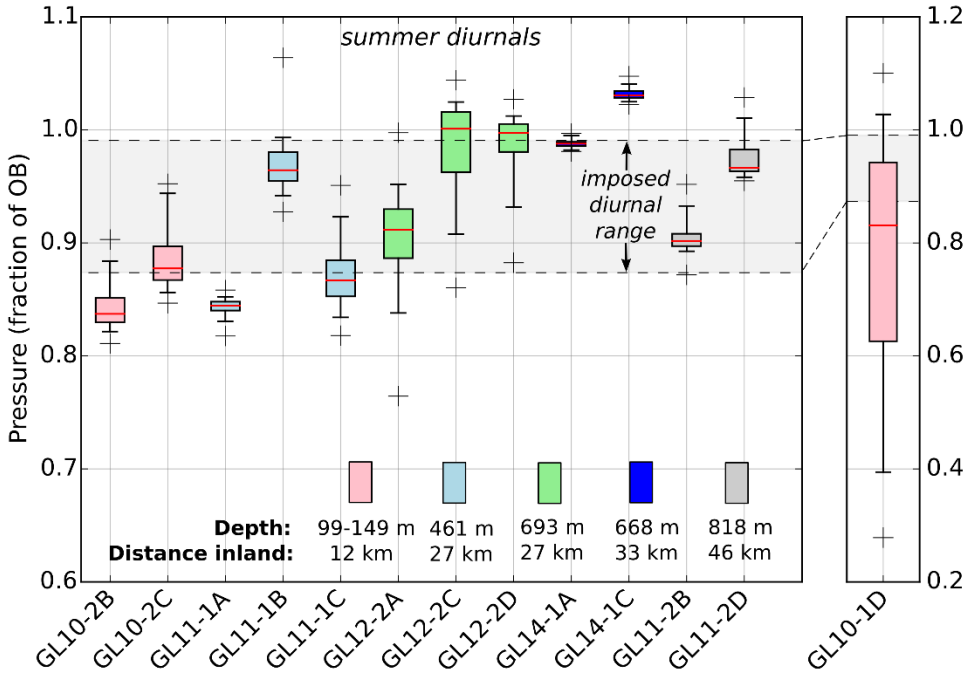

Fig. 1.10. Box plots of water pressure data for the "summer diurnal" period, where box color corresponds to distance inland. Shaded region is the imposed diurnal range used for sensitivity testing of the hydraulic potential gradient (5th to 95th percentile from borehole GL12-2C, centered at the dataset mean median). Box center lines are median, boxes span the 1st and 3rd quartiles, whiskers extend to 5th and 95th percentiles, and crosses indicate max and min points. The diurnal record for near-margin borehole GL10-1D is plotted separately at right, with the shaded region from the main panel shown for context.

The minimum and maximum values recorded in the twelve-borehole suite are 0.76 OB and 1.17 OB, respectively (shaded region in Fig. 1.9). The annual weighted mean pressure for the transect remains near overburden at 0.97 OB (Fig. 1.9, bold dashed line). This calculation of the annual mean is supported by all data in the twelve-borehole suite (data from borehole GL10-1D are not included for reasons discussed above), but this result may be biased by the weighting method, where the winter and melt season are each assigned a fixed period of the year which may be an inaccurate representation of the actual seasonal

timing for a given site. For comparison, we also present a simple calculation of annual mean pressure using only the four boreholes with year-long records. Averaging the median values of annual data re-sampled to thirty minute intervals for the full record of these boreholes, the annual mean is only 0.01 OB lower at 0.96 OB. Either treatment of the dataset therefore constrains the annul mean pressure between 0.96-0.97 OB.

1.4. Discussion

1.4.1. Representativeness of borehole pressures

The basal water pressure summary statistics presented here rely on borehole measurements that sample small areas of the bed at specific locations, and are limited to the seasonal characteristics that may be unique to the years of measurement. This brings into question how representative these results are in both time and space. Several lines of evidence, however, suggest our data are in fact broadly representative of the study region.

Borehole sites in our transect sampled multiple topographic regimes including a bedrock trough, a bedrock ridge, a relatively flat bed area away from troughs, and the wall of a major bedrock trough near the margin (Fig. 1.2). The boreholes also sampled a wide range of ice depths and distances inland from the margin (Table 1.1). Across the range of locations sampled, borehole water pressure measurements throughout the transect show similar characteristic seasonal phases and variability within a confined range of values (Fig. 1.3, 1.6, 1.9). Further, no distinct trends in pressure as a function of distance inland or ice

depth were identified. We have not, however, sampled the bottom of the very deepest bedrock trough, and the pressure regime along its main axis remains unknown.

Another concern is whether our measurements are biased by the melt conditions unique to the 2010-2015 seasons. In particular, the 2010 and 2012 melt seasons were both record warm years with large surface melt production [*Nghiem et al.*, 2012; *van As et al.*, 2012; *Tedesco et al.*, 2013]. Nevertheless, our results include three melt seasons with conditions similar to the 20-year mean surface mass balance measurements [*van de Wal et al.*, 2012]. Further, we can identify no systematic difference between water pressures measured in the high melt years and the average melt years.

Measurements of borehole water pressure at other locations across western GrIS also show similar results to those presented here (Table 1.2). Van de Wal et al. [2015] report melt season water pressure from two boreholes (spaced 5 m apart) located approximately 15 km inland and 2 km south of our transect, ranging approximately 0.92 - 1.0 OB. Andrews et al. [2014] and Ryser et al. [2014] report pressure for two melt seasons and two winters (2011-2012) from six boreholes located 20-30 km inland and 250 km northwest of our transect (~600-700 m depth). These records range approximately 0.90 – 1.13 OB, showing similar seasonal phases, and similar differences in magnitude and variability of pressure between closely spaced boreholes (30-40 m). Luthi et al. [2002] measured water pressure for two months in two deep boreholes (830 m) spaced ~20 meters apart, with weak diurnal cycles and pressure remaining steady near 1.0 OB. Earlier measurements, although

only hours to days in duration, also agree with the observations reported here. Iken et al. [1993] showed water pressure consistently near overburden (0.96 – 1.0 OB) in two ~1600 m deep boreholes 50 km inland from the terminus of the Jakobshavn outlet glacier. In addition, Thomsen and Olesen [1991] report diurnal cycles and pressures ranging 0.79 – 1.05 OB in twelve boreholes located 1-8 km from the margin (180 - 350 m depth).

An important exception to the consistency of water pressures is the record from our near-margin borehole GL10-1D. These data clearly represent a separate hydraulic regime that is an outlier in our dataset (Fig. 1.6, 1.9) and the observations of other workers. This borehole is likely not representative of overall ablation zone conditions as a result of the site location and shallow ice depth. The site is located only 450 meters from the lateral ice sheet margin where subglacial conditions are likely well-channelized and tunnels emerge at atmospheric pressure. The relatively thin ice (<100 m) limits creep closure rates, allowing increased conduit cross-sectional area and lower diurnal water pressures [*Rothlisberger*, 1972]. The large diurnal range in pressure at this site is similar to water pressure measured in mountain glacier settings [e.g. *Fudge et al.*, 2008].

To summarize, the consistency we find between multiple topographic regimes and years of measurement, as well as with all previous borehole pressure measurements for the GrIS, implies our limited point measurements are likely broadly representative of regional conditions. With exception to our shallowest near-margin borehole, water pressures throughout the transect are confined within a distinct range of relatively high pressures

(approximately 0.8–1.1 OB), and show consistent seasonal phases and a period of regular diurnal cycles. However, our results also show that within the limits of confinement, substantial local variability can be present that may not necessarily be individually upscaled to represent regional conditions.

1.4.2 Implications for hydraulic potential

Our measurements demonstrate spatial gradients in the absolute magnitude (i.e., Pa) of water pressure that arise from two components: changes in ice overburden pressure due to variable ice thickness, and changes resulting from basal drainage system processes. Computing $\nabla \phi_h$ with Equation 1 accommodates the first component by scaling measured water pressure to the ice overburden, but there are no terms to represent pressure gradients arising from other factors associated with drainage system dynamics. Our measurements reveal significant gradients in water pressure; for example, values of 20 kPa/m in holes 20 m apart (Fig. 1.7). Basal processes cause the water pressure to deviate from overburden with gradients that are not represented by bed and surface geometries alone.

Our results also indicate, however, that basal processes essentially act to modify the overburden pressure within a restricted range. With the exception of very near the margin, all time/space variability occurs within a fixed range of ~0.8 to 1.1 OB. In other words, we see no pressure gradients between points falling outside of this range of overburden

pressure. Consequently, when points 10s of km apart are considered, the dominant change in pressure arises from ice thickness differences (e.g., Fig. 1.8) and the local variability is second order at that scale. Basal process-induced gradients are further reduced by water flow paths at the bed that are likely to be longer than the straight-line connections. Thus, our transect of basal water pressure measurements implies that the far field hydraulic potential gradient mimics changes in ice thickness and basal topography, with superimposed local gradients from the basal drainage system.

Hydraulic potentials must also be considered with regards to the time variability of water pressure. Our data show that over the course of the winter, water pressures are relatively steady. Further, if one considers time steps that average over the daily melt cycle, little difference exists between the summer and winter pressures. Hence, within these time restrictions, the hydraulic potential gradient is essentially static. However, at short diurnal time scales during the peak of the melt season, swings in water pressure have the capacity to cause $\nabla \phi_h$ to be highly dynamic. Our pressure measurements across the transect reside near overburden levels, where even small fluctuations influence the relative importance of bedrock and surface topography in the calculation of the $\nabla \phi_h$ field (Fig. 1.1). In this situation, diurnal pressure changes can induce substantial cycling of both the magnitude and direction of $\nabla \phi_h$, depending on the bed and surface topography (Fig. 1.11).

To exemplify the process in the context of our study area, we explore a scenario for changing magnitude and direction of $\nabla \phi_h$ vectors using bed and surface topography at 250-meter horizontal resolution [*Lindbäck et al.*, 2014]. To impose a diurnal range in pressure, we select the largest measured 5th to 95th percentile range represented in the twelve-borehole suite (0.12 OB, borehole GL12-2C), and then center this range at the mean diurnal pressure median for all boreholes. This results in an imposed diurnal range of 0.87 to 0.99 OB (shaded region in Fig. 1.10).

Under this scenario, gradient vectors change both their magnitude and direction in response to the diurnal pressure changes. In response to an imposed pressure decline, vector magnitude increases over three quarters of the study area, with ~10% demonstrating changes of 2-3 fold (Fig. 1.12). Steeper bed slopes generally force greater increases in vector magnitude, but the greatest increase factors occur where bed slopes are relatively shallow (<20°) and corresponding surface slopes are nearly flat. Rotation over the diurnal cycle is controlled by the disparity between surface and bed slope aspects, which is commonly associated with the walls of the deep bedrock troughs. As these troughs generally trend in the direction of ice flow, their walls face normal to the surface slope.

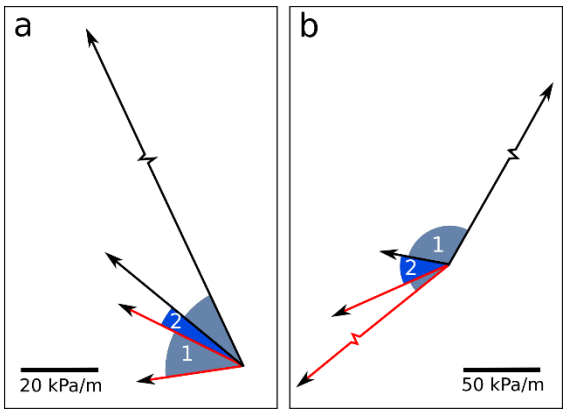

Fig. 1.11. Changes in magnitude and rotation of hydraulic potential gradient vectors resulting from the physically possible range of basal water pressure (angle 1, 0.0 OB to 1.17 OB), and for the imposed range of water pressure used for diurnal analysis (angle 2, 0.87 OB to 0.99 OB). Red vectors and black vectors correspond to high-pressure and low-pressure conditions, respectively. Panel A uses the bed and surface topography from site GL12-2A, representing conditions commonly found over steep sub-glacial trough walls where vector magnitudes increase with decreasing pressure. Panel B uses the bed and surface topography from site GL10-2C, representing conditions of reverse bed slope (bed aspect opposed to surface slope aspect), resulting in a decrease in vector magnitude with decreasing pressure.

Our imposed pressure swings are a uniform fraction of overburden across the study area; a simplification invalidated by our own data (Fig. 1.7). A more complex field of diurnal pressure swings would likely exacerbate gradients in some places, adding to the dynamic complexity of $\nabla \phi_h$. Furthermore, the very conceptualization of $\nabla \phi_h$ is complicated by whether it is defined in terms of the continuous topographic domain or the existing drainage system; the latter consisting of discrete and complex pathways across the bed. We conclude from our simplified scenario above that despite large scale water pressure gradients dominated by overburden, and the small difference between mean summer and winter pressures, short time scale diurnal variations potentially lead to dynamic alterations of a complex $\nabla \phi_h$ field.

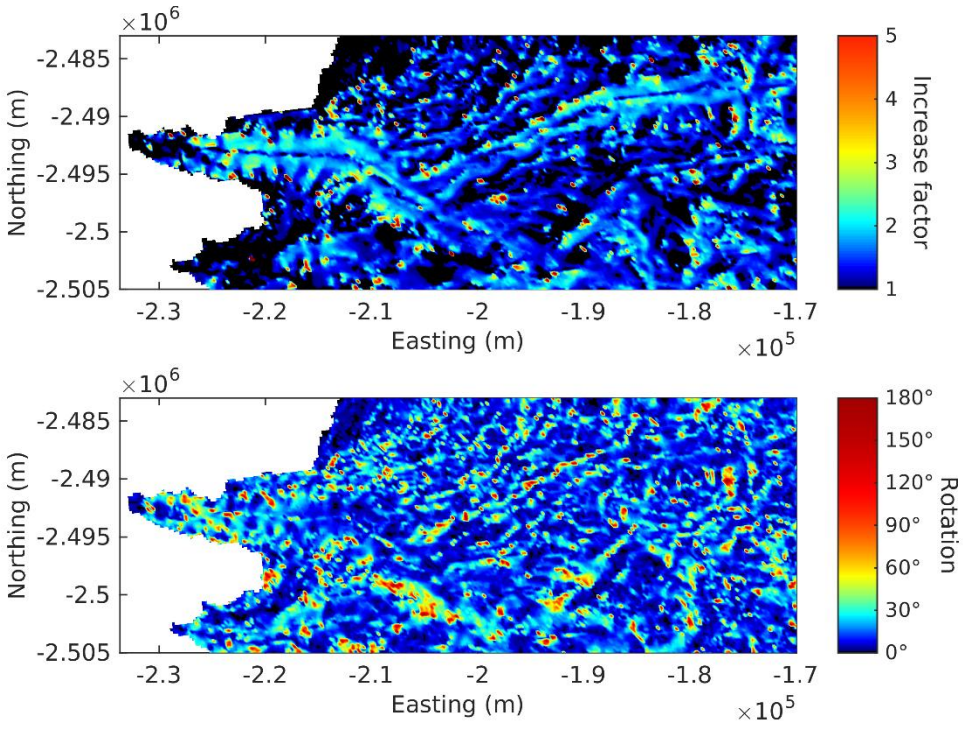

Fig. 1.12. Calculated change in magnitude (Panel A) and rotation (Panel B) of hydraulic potential gradient vectors over a diurnal cycle, using the imposed range of basal water pressure shown by the shaded region in Fig. 1.10 (0.87 OB to 0.99 OB). Black areas in Panel A indicate a decrease in gradient magnitude (factor <1.0).

1.5. Conclusions

Thirteen borehole water pressure records collected across a 46 km transect of the western Greenland Ice Sheet show that basal water pressure undergoes characteristic seasonal phases and is confined within a limited range. Water pressures are relatively steady and high during winter, variable and irregular during spring and fall, and have diurnal cycles that can persist for multiple weeks during the peak melt season. A single borehole located 450 meters from the ice sheet margin with ice depth <100 meters shows melt season water pressure ranging from 0.3 to 1.05 of overburden (OB). This record likely represents a well-

channelized hydraulic regime with high meltwater flux and limited creep closure. The remaining twelve boreholes show pressures varying within a confined range, with minimum pressure predominantly greater than 0.8 OB and maximum pressure near or just above overburden. Despite diurnal pressure changes during the summer period, melt season median pressure varies by less than 0.02 OB from winter median pressure for four of five boreholes with overwinter records.

The basal water pressure across the high relief bed of our western Greenland study area experiences gradients stemming from two sources: changes in ice thickness driving the overburden pressure, and changes arising from basal drainage processes. Because water pressure varies within a relatively restricted fraction of overburden, the hydraulic potential gradient most closely mimics the ice thickness when considered over larger spatial scales and time steps that average diurnal swings in pressure. However, on sub daily time scales during the melt season, cycling of pressure can lead to substantial changes in the direction and magnitude of the hydraulic potential gradient. Furthermore, over length scales where the ice thickness does not change substantially, the hydraulic potential is strongly influenced by large gradients resulting from basal drainage system processes.

Table 1.1 (*) indicates boreholes with over-winter records shown in Fig. 1.4 and Fig. 1.9.

Site	Latitude (°) Longitude (°)	Distance from Issun. Sermia terminus (km)	Ice depth (m)	Length of record (yyyy-mm-dd) (# days)
GL10-1D	67.162 -50.063	12	99	2010-06-15 – 2010-09-20 (98)
GL10-2B	67.167 -50.067	12	149	2010-06-22 – 2010-09-20 (91)
GL10-2C	67.167 -50.066	12	146	2010-06-26 – 2010-09-11 (78)
GL11-1A*	67.195 -49.720	27	458	2011-07-10 – 2012-07-10 (367)
GL11-1B	67.195 -49.719	27	466	2011-07-10 – 2011-09-14 (67)
GL11-1C	67.195 -49.719	27	460	2011-07-10 – 2011-09-14 (67)
GL12-2A*	67.204 -49.718	27	696	2012-06-16 – 2013-07-23 (403)
GL12-2C*	67.204 -49.718	27	688	2012-06-17 – 2013-07-16 (395)
GL12-2D*	67.204 -49.718	27	696	2012-06-21 – 2013-07-16 (391)
GL14-1A	67.182 -49.575	33	674	2014-07-17 – 2014-08-08 (23)
GL14-1C*	67.182 -49.575	33	661	2014-07-27 – 2015-04-22 (270)
GL11-2B	67.201 -49.289	46	821	2011-07-15 – 2011-09-14 (62)
GL11-2D	67.201 -49.289	46	815	2011-07-20 – 2011-09-14 (57)

Table 1.2 Summary data for all previous borehole water pressure measurements on the GrIS.

Borehole water pressure measurements on the GrIS	Pressure range (fraction of OB)	Number of boreholes*	Distance Inland** (km)	Ice Depth (m)
This study, 12-borehole suite	0.76 – 1.17	13	12 – 46	146 - 821
Van de Wal et al. (2015)	0.92 – 1.00	2	15	not reported
Andrews et al. (2014) Ryser et al. (2014)	0.90 – 1.13	6	20-30	620 – 700
Luthi (2002)	1.00-1.01	2	55	830
Iken et al. (1993)	0.96 – 1.00	2	50	1600
Thomsen and Olesen (1991)	0.79 – 1.05	12	1 – 8	180 - 350

* Number of boreholes with published water pressure records

** Distance inland is from the terminus of Issunguata Sermia (this study), or from the terminus of Jakobshavn terminus (Iken et al., 1993; Luthi et al., 2002). All other distances are approximate from the ice margin.

1.6. Supplementary Figures to Chapter 1

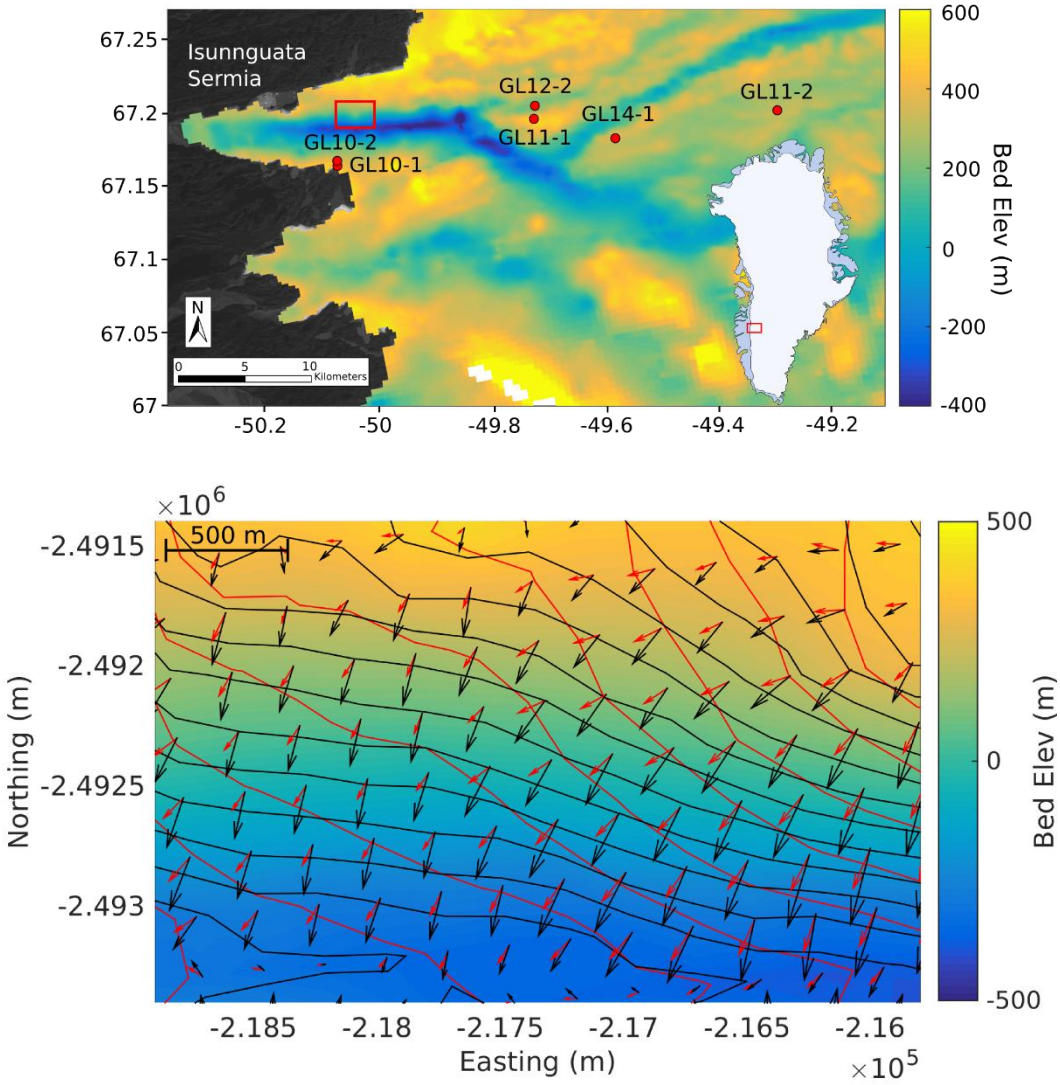

Fig. S1. Map of bed topography encompassing a steep trough wall of Issunguata Sermia outlet glacier (location indicated with inset in upper panel). Base colormap represents bed topography. Red vectors and contours represent the hydraulic potential gradient and hydraulic potential surface, respectively, for 0.99 OB pressure. Black vectors and contours represent the hydraulic potential gradient and hydraulic potential surface, respectively, for 0.87 OB pressure. The imposed pressure range corresponds to the shaded region in Fig. 1.10.

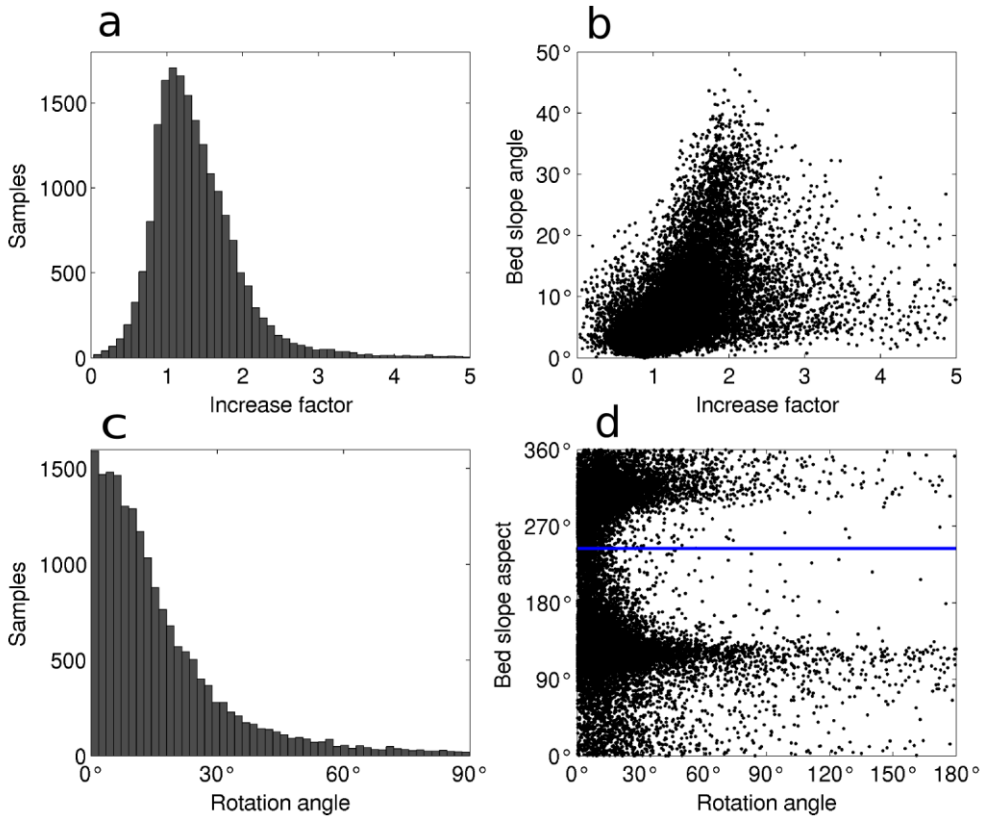

Fig. S2. Distribution of factors of magnitude change (Panel A) and vector rotation angles (Panel C) of the hydraulic potential gradient. Panels B and D show gradient vector increase factor vs. bed slope angle, and gradient vector rotation angle vs. bed slope aspect, respectively. The average ice surface slope aspect for the transect area is shown with a blue line in Panel D. Aspect of 360°/0° is north-facing, and aspect of 180° is south-facing. Analysis corresponds to the results shown in Fig. 1.12.

Supplementary figures S1 and S2 provide additional analysis of the imposed scenario of diurnal pressure cycles discussed in section 1.4.2. An analysis of vector rotation and magnitude change for a south-facing wall of the Issunguata Sermia bedrock trough (Fig. S1) represents conditions commonly found along bedrock troughs throughout the transect area. When the imposed scenario is projected across the entire study area, we find relationships between bed slope and vector increase magnitude, where increases in bed slope angle tend to promote greater increases in vector magnitude (Fig S2, B). In addition,

bed slope aspect will control the vector rotation angle, where greatest rotation occurs along walls of bedrock troughs that are predominantly opposed to surface slope aspect (Fig. S2, D).

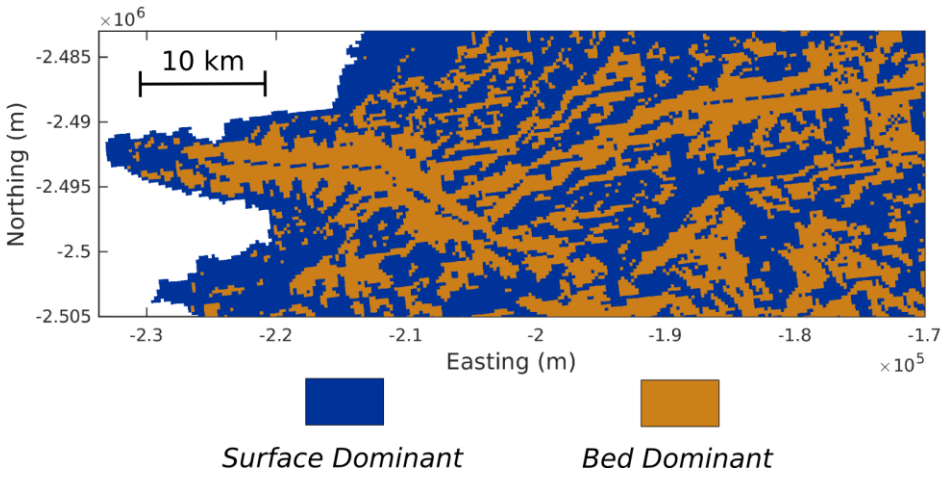

Fig. S3. Areas where surface topography (blue) or bed topography (brown) dominate the hydraulic potential gradient, calculated using water pressure of 0.94 OB (representing melt season mean pressure).

An analysis of the relative contribution of bed slopes and surface slopes to the hydraulic potential gradient demonstrates the dominance of steep bedrock terrain in the transect area (Fig. S3). As demonstrated in Equation 1 (FIg. 1.1), reduction of water pressure near overburden greatly reduces the "surface slope influence factor". Areas in brown in Fig. S3 indicate a surface factor of <1 (bed slopes are dominant), occurring for 33% of the transect area. Note that this analysis only considers DEM grid cells as surface or bed dominant in a binary fashion (even if one component only contributes slightly more), and assumes water pressure to be a spatially invariant fraction of overburden.

Chapter 2.

High time resolution measurements of surface velocity

2.1. Introduction

Surface velocity measurements were made throughout the study area using differential Global Positioning Systems (GPS) during 2010-2015. Velocity measurements provide constraints on annual, seasonal, and diurnal movement of the ice sheet surface, where the measured velocity is a combination of both basal sliding and deformational flow within the ice column. GPS measurements will be a key component of our larger science campaign to examine basal processes and the partitioning of velocity into deformation and sliding components. Here, I describe GPS station construction and electronics, data processing and post-processing steps, and provide initial velocity results for all stations.

2.2 Methods

2.2.1 GPS base and rover locations

GPS stations used in this analysis were installed at sites GL11-1, GL11-2, GL12-2, and GL14, each recording data for a period of 2-3 years (Fig. 2.1, 2.2; Table 2.2). Site descriptions (distance from margin, ice depth, and bed topography) for each rover location are included in chapter 1.2 (Fig. 1.2). Base stations used in differential processing include the Pt. 660 base station (Fig. 2.2; installed by University of Montana, July 2013), Russell base station (installed by Doyle/Hubbard, Aberystwyth University), and Kellyville base station (baseline distances for all base stations provided in Table 2.1). At site GL11-1, GL11-2, and GL12-2,

single rover stations were installed at each site. At site GL14, five GPS stations were installed in a “strain diamond” pattern, with one station in the center and four stations spanning lateral (N-S) and longitudinal (E-W) baselines of ~700 meters (Fig. 2.1).

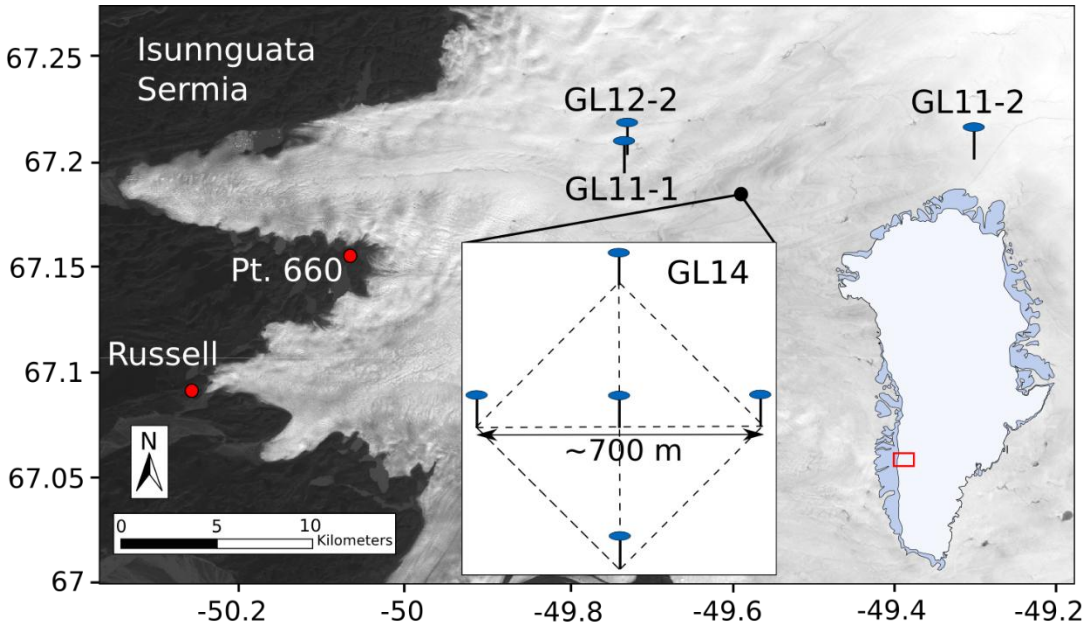

Fig. 2.1. Locations of GPS stations used in this analysis, corresponding to borehole sites shown in Fig. 1.2. The Russell and Pt. 660 GPS base stations are shown on the ice sheet margin (Kellyville is out of view to the west). Background is NASA Landsat imagery from Feb 03 2014.

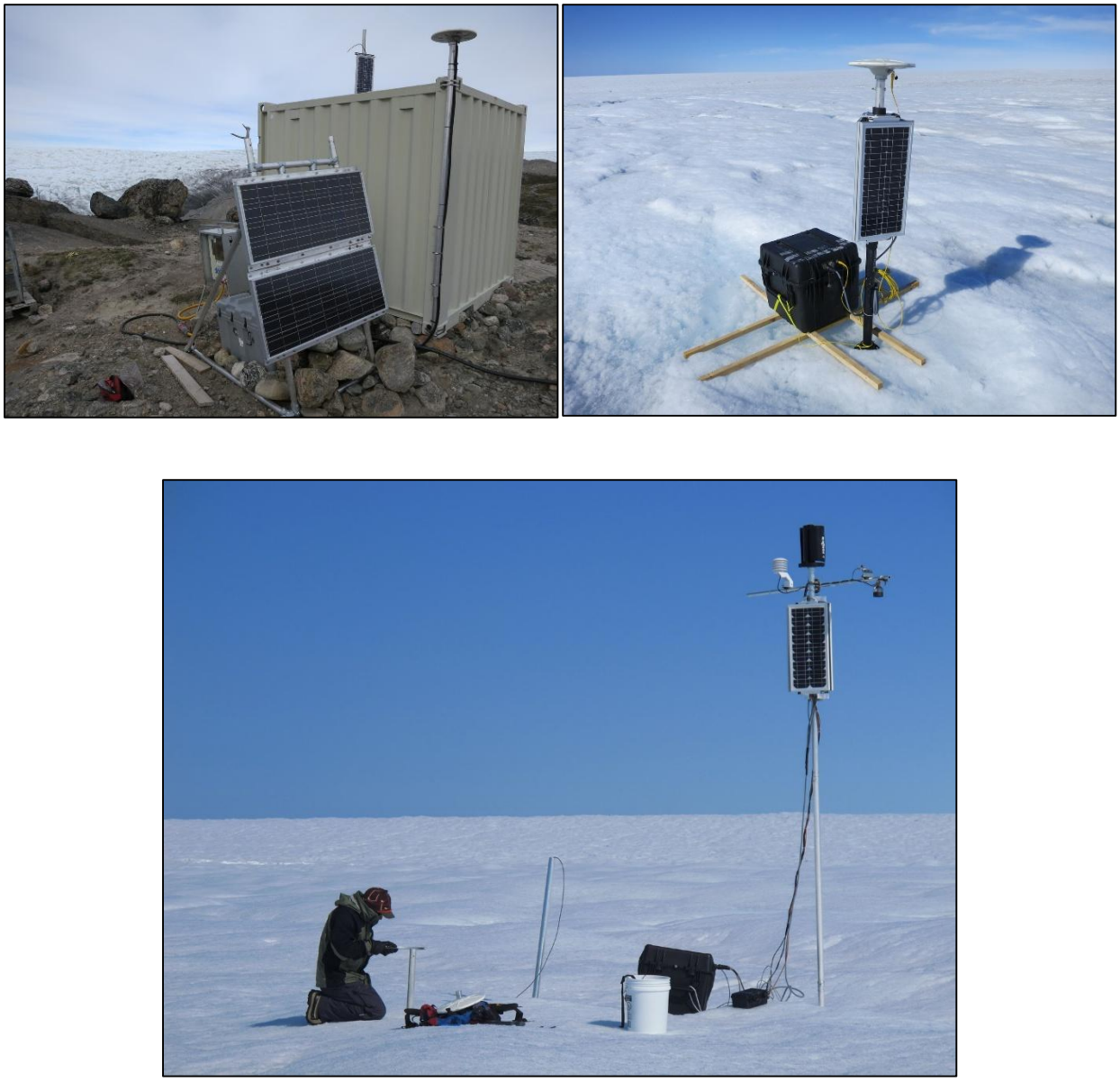

Fig. 2.2. Pt. 660 base station (upper left) and rover station at site GL14 (upper right). Elevated GPS solar panel array after extensive melting at site GL11-1 (lower).

	GL11-1	GL12-2	GL14	GL11-2
Pt. 660	15	16	21	34
Russell	26	26	31	44
Kellyville	58	58	63	76

Table. 2.1. Baseline distances (km) between all rovers and base stations.

GL11-1	GL11-2	GL12-2	GL14
20110701 – 20111031	20110712 – 20111031	20120611 – 20120918	20140715 – 20141210
20111101- 20111127	20111101 – 20111123	20130404 – 20130716	20150201 – 20150720*
20120609 – 20120918	20120623 – 20120918		
20120919 – 20121216	20121001 – 20121217		
	20130115 – 20130716		

Table. 2.2. Dates of continuous measurement for all rover stations, as 'YYYYMMDD'. Blue indicates processed against Russell base, red indicates processed against Pt. 660 base, and **black** indicates processed against Kellyville base. (* Note that continuous winter data at site GL14 was only obtained for the west station. All other stations resumed measurement after manual power-up on 20150422.)

2.2.2 Station Construction

2.2.2.1. Mechanical

The Pt. 660 base station consists of a Trimble Zephyr geodetic antenna mounted on 1 7/8" aluminum pipe, secured to the corner of the GAP bedrock borehole structure with hose clamps. Although the antenna is not mounted in bedrock (structure is built on a stacked stone foundation), the mount is sufficiently static for our processing purposes. It should be

noted that an additional solar panel mount on the northeast corner of the structure is higher than the antenna height, and could cause multiple reflection interference with the GPS signal.

All on-ice rovers use Trimble Zephyr geodetic antennas, mounted on coupled 5' sections of 1 7/8" aluminum pipe, drilled into the ice with a 5 cm Kovacs drill. Stations are initially installed with 5-6 sections of pipe, allowing the antenna mast to persist through an entire year of ablation. The solar panel array is mounted on a PVC sleeve that slides down the aluminum pipe as the ice surface lowers due to ablation. In summer 2015, wooden 2x2 crosses were lashed onto the Pelican case enclosures to prevent flipping. Issues to be aware of with this rover setup include: 1) The enclosure can slide away from the aluminum pipe, pulling tight on the tether and pulling the antenna mast out of plumb; 2) Antenna cable can fall into the ice, becoming frozen in, then pulling/breaking connectors and creating potential to damage cables when excavating them from the ice; 3) As the antenna becomes elevated with surface ablation, processing errors increase due to the antenna mast vibrating in windy conditions, particularly in winter.

2.2.2.2. Electronics

The Pt. 660 base station utilizes two large solar panels and a Flexcharge charge controller to charge a 6 x 97 Amp-hour lead-acid battery bank (582 total Ah). A Trimble NetR9 GPS receiver measures positions at 15-sec intervals. The receiver runs continuously until power

reaches a low voltage disconnect threshold of 11.0 V, with powerdown usually occurring for all of January and part of February. The base station has successfully re-powered for two consecutive winters (2013-14 and 2014-15). The antenna wire is routed through a Reactel Iridium notch filter to remove any potential interference from satellite phone signals.

Rover stations are equipped with an array of three 20-Watt solar panels and a Genasun GV-5 charge controller, charging a 4x55 Amp-hour lead-acid battery bank (220 total Ah). Measurements are made at 15-sec intervals, using Trimble NetRS or NetR9 receivers. It should be noted that the NetR9 receivers do not reliably power up in the spring, due to a firmware bug related to power cycling that can occur during the receiver shutdown procedure (T. Nylen, personal comm.). In addition, our data shows that the NetR9 receivers are susceptible to Iridium interference without a notch filter, especially at close range (<100 m).

2.2.3 Data Processing

2.2.3.1 GAMIT/GLOBK/TRACK position processing

GAMIT/GLOBK version 10.6 and TRACK version 1.28 were used for all data processing (software maintained at: www-gpsg.mit.edu/~simon/gtgk/index.htm). Pre-processing (file conversion to RINEX format) is completed with Trimble "runpkr" and UNAVCO "TEQC" software, and all satellite navigation files (.sp3) are accessed via the NASA CDDIS archive.

TRACK processing provides position and height solutions in three formats: XYZ (WGS84 cartesian coordinates), GEO (latitude/longitude/height), and NEU (north/east/up) from a user-specified local reference frame. All analysis completed here utilizes the NEU output, with positions reported either relative to the base station (default) or, for the GL14 site, to the center station position at the beginning of the period of measurement (July 15, 2014). Specific command parameters for processing can be found in the associated 'ProcessGPS_track_PJW.sh' script in the processing directories, or in the track.cmd file that is included in the processing output.

2.2.3.2 Post-processing and velocity calculations

All positional data is post-processed with the following steps: **1.** (optional) drop positions with error greater than a user-specified threshold (e.g. 5 cm), using reported TRACK error output; **2.** re-index position time-series to continuous time resolution (15-sec or 30-sec), entering NaNs for missing data. Gaps in data exist for any epoch where TRACK is unable to sufficiently resolve ambiguities, from periods of missing data from the rover or base, or due to dropped positions in step (1); **3.** use linear interpolation to fill NaNs, providing a continuous time series (required for smoothing); **4.** Perform smoothing of positions with a moving Gaussian window, using the standard Scipy implementation and specifying window length and standard deviation (Fig. 2.3); **5.** calculate velocity from smoothed positions; **6.** (optional) smooth velocity with a moving Gaussian window (Fig. 2.4).

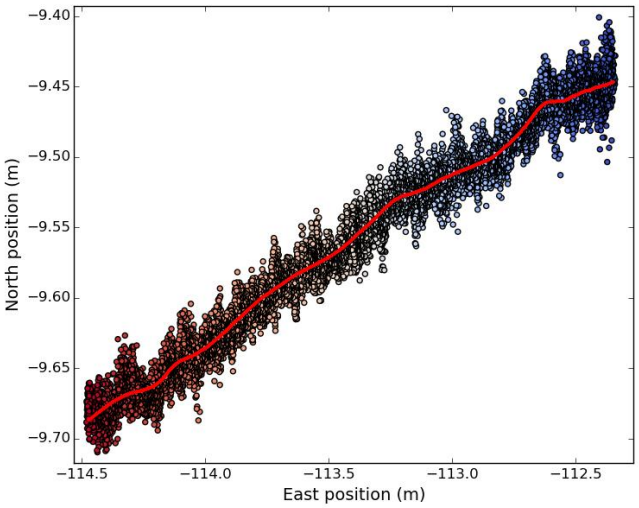

Fig. 2.3. Raw NEU positions (colored by time) for the center station at site GL14. Red line is the Gaussian-smoothed positions, with 6 hr window length, and standard deviation of 1.8 hr. Data spans July 5th through July 8th, 2015, with sense of motion from upper right (east) to lower left (west). Positions are relative to the center station position at the beginning of the 2014 campaign. Note different scales for axes.

Choices of window length and standard deviation size for both smoothing steps greatly affects the velocity output, and these values should be chosen based on the scale of analysis (i.e. diurnal, seasonal, annual). Unless otherwise stated, all velocity results presented here use 6-hr position smoothing (1.8 hr std. dev.), and 6-hr velocity smoothing (0.6 hr std. dev.).

In addition, velocity results should be trimmed by half the smoothing window length on either side of the start and stop times for station reset periods (time during which GPS antennas are lowered). This removes any velocity results that use interpolated position data during resets.

2.2.3.3 Error propagation

Although all results reported here use velocity calculated at 15-sec time intervals, proper error propagation techniques [*Taylor*, 1997] for this time-step yield uncertainty more than 2 orders of magnitude greater than the actual calculated velocity. For publication of this data, velocity calculations should be made over a larger moving window [e.g., *Bartholomew et al.*, 2011] such that uncertainty can be reduced. Choice of window length again depends on the temporal scale of analysis and the threshold for acceptable uncertainty. To calculate uncertainty in velocity, uncertainty in the change in position must first be solved as:

$$\delta x = \left[\left(\frac{\partial x}{\partial E}\delta E\right)^2 + \left(\frac{\partial x}{\partial N}\delta N\right)^2\right]^{1/2}, \quad (1)$$

where x is the total change in position, δE is uncertainty in the east component and δN is uncertainty in the north component, each solved as:

$$\delta E, \delta N = \left(\delta pos_1{}^2 + \delta pos_2{}^2\right)^{1/2}, \quad (2)$$

where δpos_1 and δpos_2 are the TRACK-reported uncertainty in positions. Uncertainty in velocity is then calculated as:

$$\delta V = \frac{\partial V}{\partial x}\delta x = \frac{1}{dt}\delta x, \quad (3)$$

where δV is uncertainty in velocity, δx is uncertainty in the change in position, and dt is the time-step for velocity calculation (moving window length). Therefore, uncertainty in velocity is highly dependent on dt, as δx will be relatively constant within the range of position uncertainty (usually 1.5-3 cm). Assuming a position uncertainty of 1.5 cm, a velocity of 103 m/yr (approximate winter background velocity) calculated with a 6-hr moving window will yield an uncertainty of ~31 m/yr. Velocities calculated with a larger window size do not yield significantly different results than smoothing with the same window size from 15-sec velocity (Fig. 2.4), however the difference between the two timeseries could be important depending on the scale of analysis (i.e. at semidiurnal scales in Fig. 2.4).

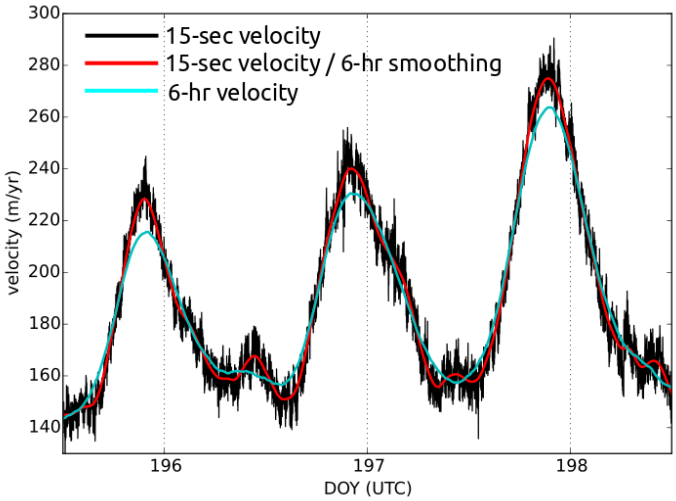

Fig. 2.4. Velocity for the center station at site GL14 during summer 2015. Velocity can be calculated directly from 15-sec smoothed positions (black), then smoothed with a 6-hr Gaussian window (red), or calculated directly from smoothed positions with a 6-hr Gaussian window (cyan). The latter method provides reduced uncertainty.

2.3. Results

2.3.1. Seasonal phases

2.3.1.1 Melt season

Velocity records show two distinct seasonal phases defining the melt season and winter. The melt season usually spans late June to early September, defining a period of higher variability and increased velocity over the winter background velocity (Fig. 2.5).

For the two sites with continuous spring speedup records (GL12-2, GL14) the transition out of the winter period occurs as a relatively slow increasing ramp over a 5-6 day period, with a gradually increasing range of diurnal variability. The early part of the melt season (late June to early July) shows distinct but irregular diurnal cycles at all sites, with the highest velocity peaks of the season generally reached during this period (maximum velocities of 250-375 m/yr). Site GL12-2 is an exception, however, which shows sustained diurnal maximums throughout the melt season.

A period of regular and strong diurnal cycles is reached during mid-summer at almost every site, where diurnal cycles typically range from minimums of 100-150 m/yr to maximums of 200–250 m/yr. However, periods of regular diurnal cycles are usually not sustained for much longer than a week before transitioning to multiday dampening or multiday speedup events. The summer 2012 record at site GL11-2 is an obvious outlier, lacking any period of regular diurnal cycles, but instead defined by large and episodic multiday speedup events throughout the season, reaching maximum velocities over 350 m/yr (Fig. 2.5, panel B). Overall, the melt season shows a declining trend in velocities at all

sites. This is visually most evident in the records as a declining baseline of diurnal minimums, but is also present as a declining trend for linear regression lines calculated for all melt season data at each site (Fig. 2.5). Despite high diurnal maximums, melt season median velocity is typically elevated over winter background velocity by only 20-30 m/yr (Table 2.3).

The timing of diurnal cycles during the melt season is very consistent throughout the transect. Velocity maximums occur between 20:00 – 22:00 UTC, and velocity minimums occur between 08:00 – 10:00 UTC (e.g. Fig. 2.6). Semidiurnal signals are also present in the smoothed velocity time series, however at the time of this analysis it is not clear whether these signals are real or artifacts of data processing.

Continuous records of the fall transition have been measured at every site, providing excellent characterization of this period. Velocities during late August and September are highly irregular, defined by dampening diurnal cycles which are periodically interrupted by distinct multiday speedup events. Every site shows 1-2 late season speedup events where velocity is rapidly ramped to maximums typically over 200 m/yr, which are then sustained for 1-4 days before returning to velocities near the winter background magnitude.

2.3.1.2 Winter

Two sites show winter records spanning from the fall into spring of the following year (GL11-2, GL14), with data gaps occurring for periods of station power-down during

December, January, and February (Fig. 2.7). All other sites show discontinuous records during the fall that are not shown in these results. The winter period is characterized by sustained velocities of ~95-120 m/yr, with sites GL11-2 and GL14 showing winter medians of 103 m/yr and 112 m/yr, respectively (Table 2.3). Velocity records over winter can show low-amplitude diurnal and semi-diurnal cycles, however it is not clear at the time of this analysis whether these are real signals or artifacts of the data processing. Over-winter records show distinct increasing trends, with both sites increasing by ~10-20 m/yr over the course of the winter (Fig. 2.7). Winter velocities dominate nearly 9-10 months of the year, and thus largely influence annual motion. Melt season and winter records spanning a full annual period were obtained at sites GL11-2 and GL14 (Fig. 2.8).

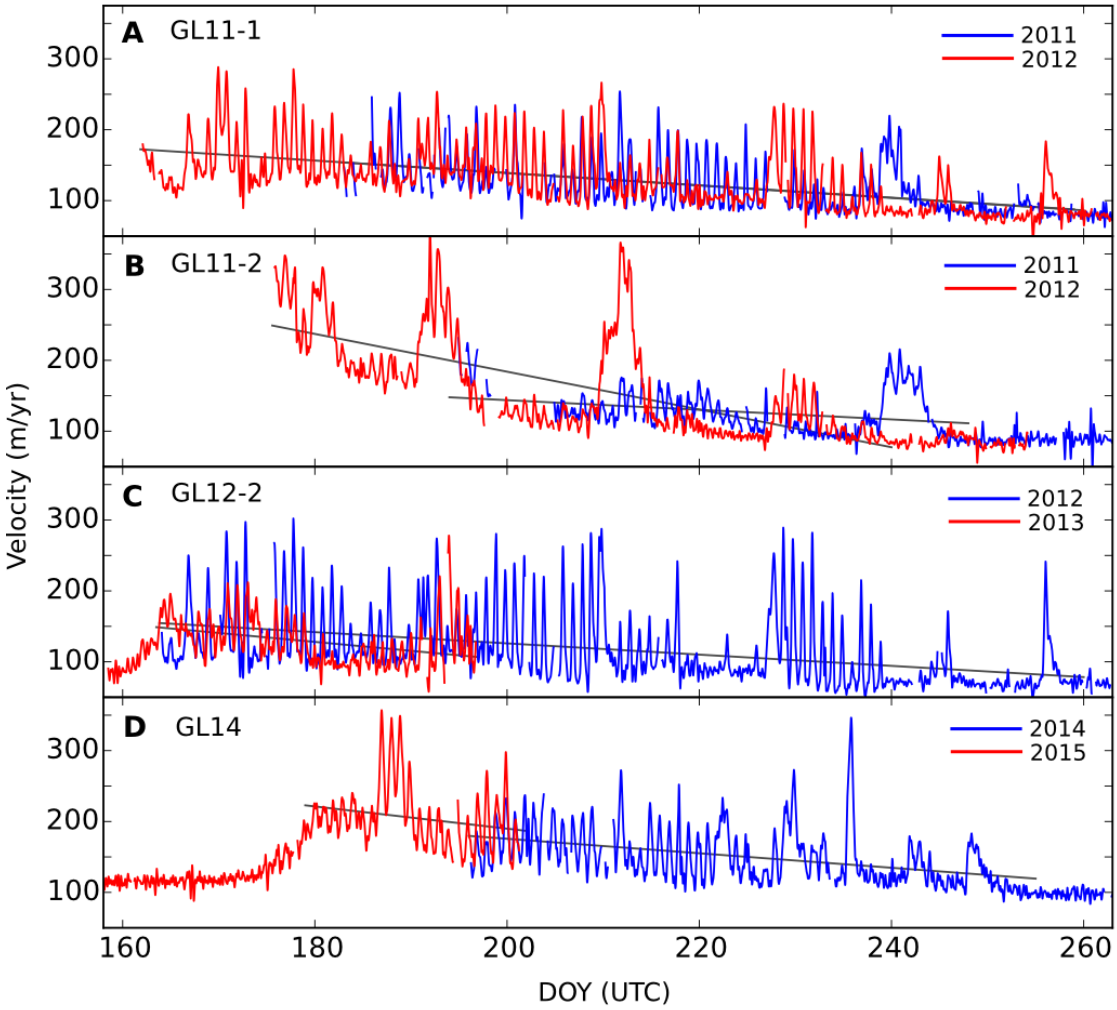

Fig. 2.5. Melt season GPS velocity records for all sites, where each site shows two consecutive partial or complete records. Linear regression lines for all data in the characteristic melt season period are shown for each record. All processing is against the Russell base station, except the 2013 GL12-2 record (against Kellyville), and the GL14 records (against Pt. 660).

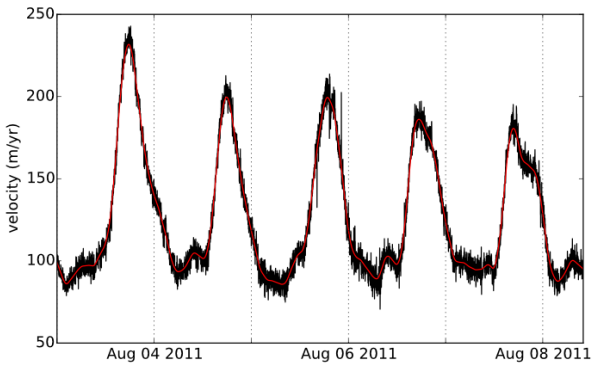

Fig. 2.6. Five day period of diurnal velocity cycles during August at site GL11-1. The timing of diurnal maximums and minimums is very consistent throughout the transect.

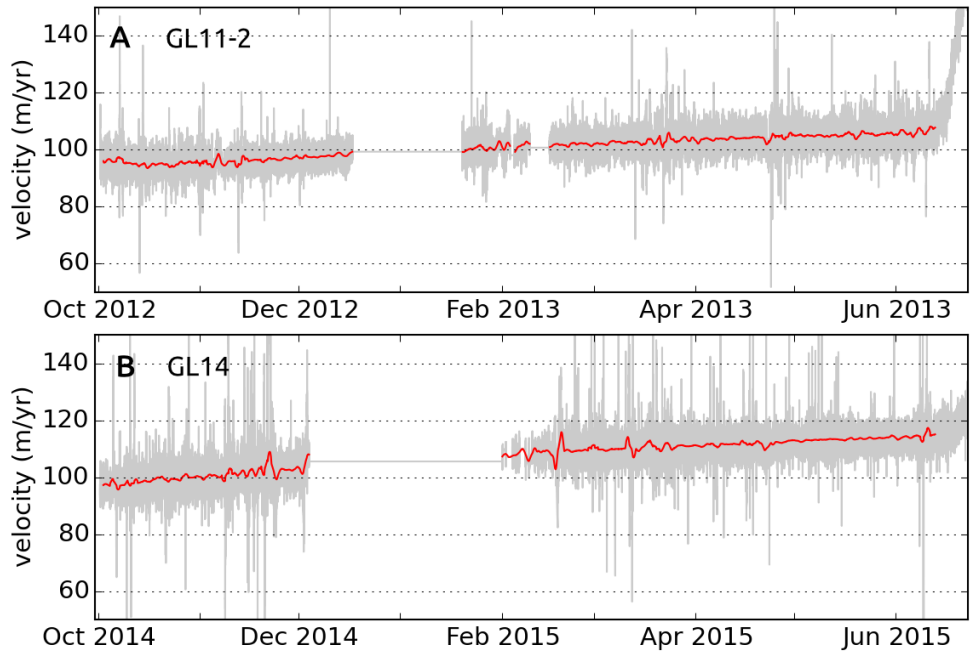

Fig. 2.7. Winter GPS velocity records for sites GL11-2 (panel A) and GL14 (panel B). Velocity is calculated directly from 24-hr smoothed positions (grey) and then smoothed with a 48-hr Gaussian window (red). Discontinuous sections of data result from mid-winter power-down periods for the base station and/or rovers. Large excursions in the data are likely due to processing-related noise, or from poor rover data resulting from elevated antennas during windier winter months. Site GL11-2 is processed against Kellyville base station, and site GL14 is processed against Pt. 660 base station.

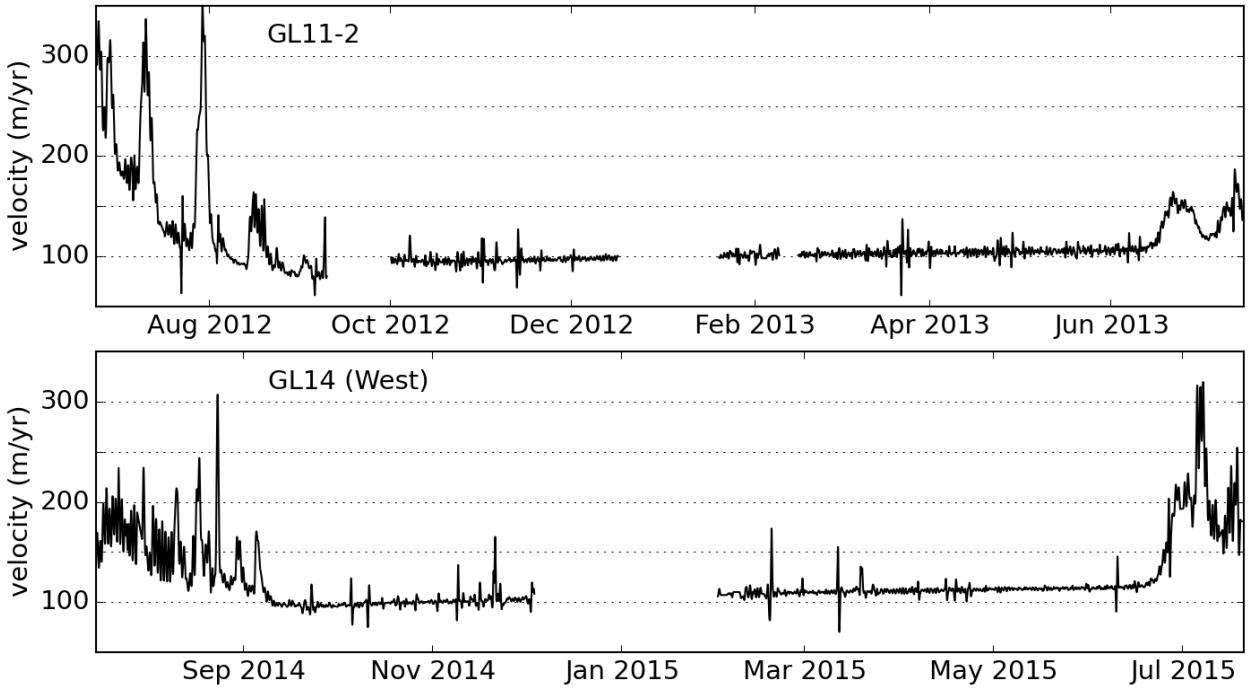

Fig. 2.8. Full annual records for sites GL11-2 (20120623 – 20130716) and GL14, west station (20140715 – 20150720), where winter periods correspond to those shown in Fig. 2.7. Periods of missing data are due to over-winter power-down. Positions and velocity both smoothed with a 12-hr Gaussian window. Large deviations that appear symmetric around the velocity baseline are interpreted as error (noise).

2.3.2 Between-station comparisons

2.3.2.1. Spatial and temporal variability throughout transect

There are no clear spatial trends in velocity between sites as a function of distance from margin or ice depth. However, basic spatial observations from the melt season dataset (Fig. 2.5) indicate:

- Velocity is highly variable at the scale of 10s of kms. For a given melt season, each site's record tends to be unique to the location. This is particularly true for the inland site GL11-2, showing damped diurnal cycles and large episodic multiday events in both years of record, as compared to more regular and larger magnitude diurnal cycles at other sites.
- At the scale of 1 km spacing, velocity between sites is very consistent in timing, but can be variable in magnitude. For example, the 2012 records of sites GL11-1 (ridge site) and GL12-2 (trough site), are very similar in timing, duration, and behavior of velocity events throughout the melt season. However, the relative magnitude of each feature in the velocity record is greater at site GL12-2 (peaks of 250-300 m/yr at GL12-2 vs. peaks of 200-250 m/yr at GL11-1). The velocity records between stations at site GL14 further confirm these results for consistency in spatial variability at scales <1 km.
- Sites furthest inland (GL11-2 and GL14) show the highest diurnal maximum velocities of the dataset (near 375 m/yr) and also show the highest median melt season velocities of the dataset (ranging 134-142 m/yr, excluding the partial spring 2015 record at site GL14). Site GL12-2 (trough site) shows the lowest diurnal minimum velocities of the dataset (near 50 m/yr), and the lowest median melt season velocity (106 m/yr) (Table 2.3).

Analysis of temporal variability can be completed for two consecutive melt season records at each site (with exception to site GL14 which only has a short period of overlapping melt season data from 2014 and 2015) (Fig. 2.5). Velocity for each melt season tends to be

highly unique for a given site. For example, site GL11-1 has an almost identical linear regression fit for 2011 and 2012 melt season data, yet the relative magnitude and timing of major features of the record is very different from one season to the next. At sites GL11-1, GL11-2, and GL12-2, the 2012 melt season shows considerably higher maximum diurnal velocities compared to 2011 or 2013, which could be attributed to the record warm air temperatures and melt production during 2012 [*Nghiem et al.*, 2012; *Tedesco et al.*, 2013]. It should also be noted that the analysis of temporal variability from season to season is affected by site locations that move by ~100 m/yr, possibly migrating to different velocity regimes.

2.3.2.2. Spatial variability within the GL14 strain diamond

Stations within the strain diamond demonstrate that overall magnitude and variability of surface velocity are very consistent at the scale of 100s of meters (Fig. 2.9). However, individual maxima and minima typically vary by 10-20 m/yr between stations, creating slight gradients in surface velocity over the area of the diamond. Throughout the 2014 melt season record, the south station typically shows the highest diurnal maxima, and the north station shows the lowest diurnal maxima. Patterns for diurnal minima are less consistent, although the north station generally continues to set the lowest minimums. In 2015, this spatial pattern is not as strong, although the north station again generally shows the lowest diurnal minima and maxima throughout the melt season.

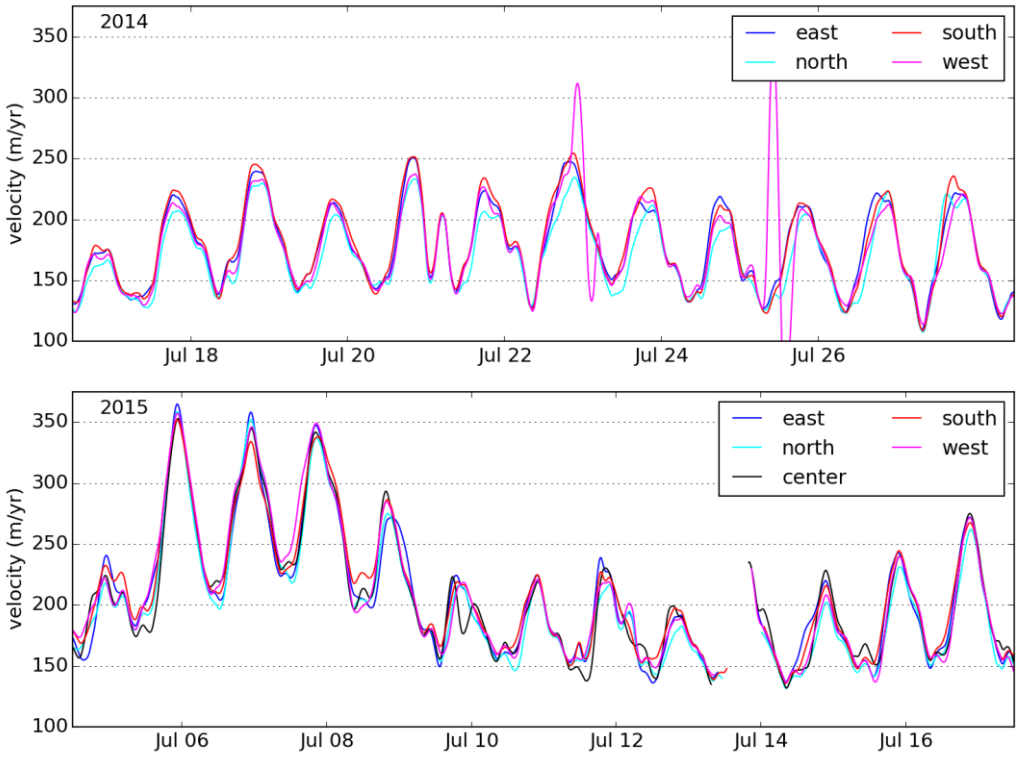

Fig. 2.9. GPS velocity records during the 2014 (upper panel) and 2015 (lower panel) melt seasons from five stations in the "strain diamond" at site GL14. Panels span ~12 day periods to show details of spatial variability between stations. Records for the center station in 2014 are not included due to high noise from Iridium satellite phone interference. Large excursions in the west station velocity for 2014 are considered to be error (noise).

	GL11-1	GL11-2	GL12-2	GL14
melt season median	*2011*: 118 *2012*: 127	*2011*: 134 *2012*: 138	*2012*: 106 *2013**: 123	*2014*: 142 *2015**: 202
winter median	N/A	*2012-13*: 103	N/A	*2014-15*: 112

Table 2.3. Melt season and winter median velocities (m/yr) for all stations. (*) indicates partial record that ends in mid-July.

2.4. Discussion

2.4.1 Water pressure and surface velocity

GPS surface velocity records and borehole water pressure records (Ch. 1) generally show similar seasonal phases and timing of transitions between phases at each site. As demonstrated in the melt season velocity (Fig. 2.5) and pressure (Fig. 1.3, 1.4) records, both time series show distinct spring transitions, periods of strong mid-summer diurnal cycles, and irregular periods of higher variability and dampening of diurnals in the fall. An exception to this general similarity is found in the behavior of the spring transition: velocity tends to show a slower multiday increasing ramp transitioning from winter background velocities to melt season behavior (Fig. 2.5, Panels C and D; Fig. 2.8), whereas basal pressure almost always initiates in the spring with a sudden event (rapid increase over hours) (e.g. Fig. 1.3).

Initial analysis also shows site-specific relationships between diurnal cycles of pressure and velocity. Diurnal hysteresis and both correlation and anti-correlation between pressure and velocity are demonstrated in the data. Sites GL14, GL11-1, and GL11-2 generally show the timing of velocity to be anti-correlated (out of phase) with pressure, whereas site GL12-2 shows velocity well-correlated (in phase) with pressure. In addition, pressure and velocity at site GL12-2 both show the largest diurnal ranges among corresponding datasets from other sites.

2.5. Summary and Conclusions

High time resolution GPS surface velocity records were collected at 4 sites along a transect on the western Greenland icesheet during 2011-2015, providing at least two consecutive melt season velocity records at each site, and over-winter records at two sites. Data was processed with TRACK v.1.28 at 15 sec or 30 sec epochs against base stations including Kellyville (baselines ranging 58-76 km), Russell (baselines ranging 26-44 km), and Pt. 660 (baselines ranging 15-34 km).

Velocity at all sites shows seasonal phases including: a multi-day increasing ramp in the spring from winter background velocities; a period of regular diurnal cycles during mid-summer; and a period of more irregular and variable behavior in the fall, typically characterized by episodic single- or multi-day speedup events. At all sites, linear regression shows decreasing trends in velocity over the melt season. Winter velocity at two sites (GL11-2 and GL14) has magnitude of ~100-120 m/yr, and persists for 9-10 months of the year. In both over-winter records, velocity slowly increases by 10-20 m/yr over the course of the winter.

Velocity from site to site is highly variable at the scale of 10s of kilometers, whereas at the scale of 100s of meters up to 1 km, the general features of the velocity record are very similar between sites. However, the magnitude of diurnal cycle maximums will vary at these spatial scales, ranging from 10-20 m/yr variability at 700-meter spacing (site GL14), to 50-100 m/yr variability at 1 km spacing (sites GL11-1 and GL12-2). Large temporal variability between consecutive melt seasons is present for each site, particularly for the 2012 melt season in comparison to 2011 and 2013.

References

Andrews, L. C., G. A. Catania, M. J. Hoffman, J. D. Gulley, M. P. Lüthi, C. Ryser, R. L. Hawley, and T. A. Neumann (2014), Direct observations of evolving subglacial drainage beneath the Greenland Ice Sheet, *Nature*, *514*(7520), 80–83, doi:10.1038/nature13796.

van As, D., A. L. Hubbard, B. Hasholt, A. B. Mikkelsen, M. R. van den Broeke, and R. S. Fausto (2012), Large surface meltwater discharge from the Kangerlussuaq sector of the Greenland ice sheet during the record-warm year 2010 explained by detailed energy balance observations, *Cryosph.*, *6*(1), 199–209, doi:10.5194/tc-6-199-2012.

Bamber, J. L. et al. (2013), A new bed elevation dataset for Greenland, *Cryosphere*, *7*(2), 499–510, doi:10.5194/tc-7-499-2013.

Bartholomew, I. D., P. Nienow, A. Sole, D. Mair, T. Cowton, M. A. King, and S. Palmer (2011), Seasonal variations in Greenland Ice Sheet motion: Inland extent and behaviour at higher elevations, *Earth Planet. Sci. Lett.*, *307*, 271–278.

Catania, G. A., and T. A. Neumann (2010), Persistent englacial drainage features in the Greenland Ice Sheet, *Geophys. Res. Lett.*, *37*(2), doi:10.1029/2009GL041108.

Chandler, D. M. et al. (2013), Evolution of the subglacial drainage system beneath the Greenland Ice Sheet revealed by tracers, *Nat. Geosci.*, *6*(3), 195–198, doi:10.1038/ngeo1737.

Cuffey, K. M., & Paterson, W. S. B. (2010), *The physics of glaciers*, 4th edition, Academic Press.

Das, S. B., I. Joughin, M. D. Behn, I. M. Howat, M. A. King, D. Lizarralde, and M. P. Bhatia (2008), Fracture Propagation to the Base of the Greenland Ice Sheet During Supraglacial Lake Drainage, *Sci.* , *320* (5877), 778–781, doi:10.1126/science.1153360.

Dow, C. F., B. Kulessa, I. C. Rutt, S. H. Doyle, and A. Hubbard (2014), Upper bounds on subglacial channel development for interior regions of the Greenland ice sheet, *J. Glaciol.*, *60*(224), 1044–1052, doi:10.3189/2014JoG14J093.

Fudge, T. J., N. F. Humphrey, J. T. Harper, and W. T. Pfeffer (2008), Diurnal fluctuations in borehole water levels: configuration of the drainage system beneath Bench Glacier, Alaska, USA, *J. Glaciol.*, *54*(185), 297–306, doi:10.3189/002214308784886072.

Harrington, J. A., N. F. Humphrey, and J. T. Harper (2015), Temperature distribution and thermal anomalies along a flowline of the Greenland ice sheet, *Ann. Glaciol.*, *56*(70), 98–104, doi:10.3189/2015AoG70A945.

Hewitt, I. J. (2013), Seasonal changes in ice sheet motion due to melt water lubrication, *Earth Planet. Sci. Lett.*, *371-372*, 16–25, doi:10.1016/j.epsl.2013.04.022.

Hewitt, I. J., C. Schoof, and M. A. Werder (2012), Flotation and free surface flow in a model for subglacial drainage. Part 2. Channel flow, *J. Fluid Mech.*, *702*, 157–187, doi:10.1017/jfm.2012.166.

Hoffman, M. J., G. A. Catania, T. A. Neumann, L. C. Andrews, and J. A. Rumrill (2011), Links between acceleration, melting, and supraglacial lake drainage of the western Greenland Ice Sheet, *J. Geophys. Res.*, *116*(F4), F04035, doi:10.1029/2010JF001934.

Iken, A., K. Echelmeyer, W. Harrison, and M. Funk (1993), Mechanisms of fast flow in Jakobshavns Isbrae, West Greenland: Part I. Measurements of temperature and water level in deep boreholes, *J. Glaciol.*, *39*(131), 15–25.

Lewis, S. M., and L. C. Smith (2009), Hydrologic drainage of the Greenland ice sheet, *Hydrol. Process.*, *23*(14).

Lindbäck, K., R. Pettersson, S. H. Doyle, C. Helanow, P. Jansson, S. S. Kristensen, L. Stenseng, R. Forsberg, and A. L. Hubbard (2014), High-resolution ice thickness and bed topography of a land-terminating section of the Greenland Ice Sheet, *Earth Syst. Sci. Data*, *6*(2), 331–338, doi:10.5194/essd-6-331-2014.

Lindbäck, K., R. Pettersson, A. L. Hubbard, S. H. Doyle, D. van As, A. B. Mikkelsen, and A. A. Fitzpatrick (2015), Subglacial water drainage, storage, and piracy beneath the Greenland ice sheet, *Geophys. Res. Lett.*, *42*(18), 7606–7614, doi:10.1002/2015GL065393.

Liston, G. E., and S. H. Mernild (2012), Greenland Freshwater Runoff. Part I: A Runoff Routing Model for Glaciated and Nonglaciated Landscapes (HydroFlow), *J. Clim.*, *25*(17), 5997–6014, doi:10.1175/JCLI-D-11-00591.1.

Livingstone, S. J., C. D. Clark, J. Woodward, and J. Kingslake (2013), Potential subglacial lake locations and meltwater drainage pathways beneath the Antarctic and Greenland ice sheets, *Cryosph.*, *7*(6), 1721–1740, doi:10.5194/tc-7-1721-2013.

Luthi, M., M. Funk, A. Iken, S. Gogineni, and M. Truffer (2002), Mechanisms of fast flow in Jakobshavn Isbrae, West Greenland: Part III. Measurements of ice deformation, temperature and cross-borehole conductivityin boreholes to the bedrock, *J. Glaciol.*, *48*(162), 369–385, doi:10.3189/172756502781831322.

McGrath, D., W. Colgan, K. Steffen, P. Lauffenburger, and J. Balog (2011), Assessing the summer water budget of a moulin basin in the sermeq avannarleq ablation region, Greenland ice sheet, *J. Glaciol.*, *57*(205), 954–964, doi:10.3189/002214311798043735.

Meierbachtol, T., J. Harper, and N. Humphrey (2013), Basal Drainage System Response to Increasing Surface Melt on the Greenland Ice Sheet, *Science*, *341*(6147), 777–779.

Morlighem, M., E. Rignot, J. Mouginot, H. Seroussi, and E. Larour (2014), Deeply incised submarine glacial valleys beneath the Greenland ice sheet, *Nat. Geosci.*, *7*(6), 18–22, doi:10.1038/ngeo2167.

Nghiem, S. V., D. K. Hall, T. L. Mote, M. Tedesco, M. R. Albert, K. Keegan, C. A. Shuman, N. E. DiGirolamo, and G. Neumann (2012), The extreme melt across the Greenland ice sheet in 2012, *Geophys. Res. Lett.*, *39*(20), 6–11, doi:10.1029/2012GL053611.

Rothlisberger, H. (1972), Water pressure in intra- and subglacial channels, *J. Glaciol.*, *11*(62).

Ryser, C., M. P. Lüthi, L. C. Andrews, G. A. Catania, M. Funk, R. Hawley, M. J. Hoffman, and T. A. Neumann (2014), Caterpillar-like ice motion in the ablation zone of the Greenland ice sheet, *J. Geophys. Res.*, 2258–2271, doi:10.1002/2013JF003067.

Shreve, R. L. (1972), Movement of water in glaicers, *J. Glaciol.*, *11*(62), 205–214.

Taylor, J. R. (1997), *An Introduction to Error Analysis: The Study of Uncertainties in Physical Measurements*, 2nd ed., University Science Books.

Tedesco, M., X. Fettweis, T. Mote, J. Wahr, P. Alexander, J. E. Box, and B. Wouters (2013), Evidence and analysis of 2012 Greenland records from spaceborne observations, a regional climate model and reanalysis data, *Cryosph.*, *7*(2), 615–630, doi:10.5194/tc-7-615-2013.

Tedstone, A. J., P. W. Nienow, N. Gourmelen, and A. J. Sole (2014), Greenland ice sheet annual motion insensitive to spatial variations in subglacial hydraulic structure, *41*(24), 8910–8917, doi:10.1002/2014GL062386.Received.

Thomsen, H.H., Olesen, O.B., Braithwaite, R.J., Boggild, C. E. (1991), Ice drilling and mass balance at Pakitsoq, Jakobshavn, central West Greenland, *Rapp. Gronl. Geol. Unders*, *152*, 80–84.

Thomsen, H.H., Oleson, O. B. (1990), Continued glaciological investigations with respect to hydropower and ice-climate relationships at Pakitsoq, Jakobshavn, West Greenland, *Rapp. Gronl. Geol. Unders*, *148*, 83–86.

Thomsen, H.H., Oleson, O. B. (1991), Hydraulics and hydrology on the Inland Ice, *Rapp. Gronl. Geol. Unders.*, *152*, 36–38.

van de Wal, R. S. W., W. Boot, C. J. P. P. Smeets, H. Snellen, M. R. van den Broeke, and J. Oerlemans (2012), Twenty-one years of mass balance observations along the K-

transect, West Greenland, *Earth Syst. Sci. Data*, *4*(1), 31–35, doi:10.5194/essd-4-31-2012.

van de Wal, R. S. W. et al. (2015), Self-regulation of ice flow varies across the ablation area in south-west Greenland, *Cryosph.*, *9*(2), 603–611, doi:10.5194/tc-9-603-2015.

Werder, M. A., I. J. Hewitt, C. G. Schoof, and G. E. Flowers (2013), Modeling channelized and distributed subglacial drainage in two dimensions, *J. Geophys. Res. Earth Surf.*, *118*(4), 2140–2158, doi:10.1002/jgrf.20146.